Evaluation of Hurricane Wind Speed Analyses in a Simulation of Hurricane Earl (2010) Using Low-Order Wavenumbers

GEORGE ANDREW SOUKUP AND FRANK D. MARKS

NOAA/AOML/Hurricane Research Division, Miami, Florida

ABSTRACT

To determine how well a low-order wavenumber representation describes a hurricane wind speed field, given its natural variability in space and time, low-order wavenumber representations were calculated for hourly "snapshots" of the 10-m wind speed field generated by the current operational hurricane model. Two distinct periods were examined: the first when the storm is in a reasonably steady state over 7–8 h and the second where the storm is changing its internal structure over a similar time interval. Observing system sensitivity experiments were also performed using wind speed field time series obtained from interpolation of the model snapshots for each of the two periods. The time series were sampled along the flight legs of a typical "figure four" aircraft flight pattern to simulate the surface wind data collection process to ascertain the effects of the wind speed field's temporal and spatial variability upon the low-order wavenumber analyses.

The comparison between the model wind speed field at any time and the wavenumber representations during the "steady state" period shows that the essential features of the wind speed field are captured by wavenumbers 0 and 1 and that including up to wavenumber 3 practically reproduces the model field. However, in the "nonsteady" period the wavenumber 0 and 1 representation is frequently unable to capture the essential characteristics of the wind speed field. The observing system sensitivity experiments suggest that when the primary circulation is rapidly changing in amplitude and/or structure during the data collection period, the low-order wavenumbers analysis of the wind speed field will only represent the temporal mean structure.

1. Introduction

To describe the structure of the hurricane horizontal wind field at Earth's surface, the most reliable surface measurements should be utilized. At present, the wind measurements obtained from the stepped frequency microwave radiometer (SFMR; Uhlhorn and Black 2003), global positioning system (GPS) dropwindsonde (Hock and Franklin 1999), and buoy measurements are considered the most reliable. The dropwindsonde and buoy data are normally available at the surface (10 m) level only at a limited number of locations and usually in a small region of the hurricane wind field. SFMR measurements, by contrast, are available over an extended aircraft flight path. Surface (10 m) wind speed measurements are collected along the aircraft flight path, providing an effective along-track resolution of about 1.3 km (Fig. 7; Uhlhorn and Nolan 2012). The usual flight pattern is a "figure four," which provides two complete orthogonal passes through the storm,

augmented by a downwind section joining the end of the second and beginning of the third orthogonal legs (Fig. 1). The quality and quantity of the wind speed measurements so obtained allow the approximate determination of the wavenumber 0 and 1 components of the Earth-relative hurricane wind speed field in a storm relative coordinate system.

The determination is quite good in cases where the first two wavenumbers dominate the higher-order wavenumbers, so that spatial aliasing is minimal (e.g., Reasor et al. 2000; Uhlhorn and Nolan 2012; Lorsolo and Aksoy 2012; Vukicevic et al. 2014). Uhlhorn and Nolan (2012) examined the question of sampling on the estimate of the peak surface wind using a high-resolution simulation of Hurricane Isabel as "nature" to generate synthetic SFMR surface and flight-level wind observations for a standard figure-four flight pattern. Using the synthetic observations, they examined the impact of spatial resolution and temporal sampling on the analysis of the peak surface wind using 97 instantaneous hourly 10-m wind snapshots. They showed that wavenumber 0 was roughly 83% of the peak 1-min-average wind speed and 88% of the 10-min-average

Corresponding author: Frank D. Marks, frank.marks@noaa.gov

wind speed. They also found that the maximum observed surface wind speed measured by an SFMR-equipped aircraft typically underestimates the storm's maximum 1-min sustained wind speed by 7%–10%, on average. They pointed out that their result was subject to the ability of the model to simulate real surface wind speed features corresponding to the proper time and space scales.

Vukicevic et al. (2014) described a new metric consisting of the sum of amplitudes of azimuthal wavenumbers 0 and 1 for wind speeds within the TC vortex and a stochastic residual at the radius of maximum wind. The residual wind speed is defined as the difference between the 1-min sustained wind speed and the sum of the amplitudes of wavenumbers 0 and 1. They examined the time evolution of wavenumbers 0 and 1 as the vortex evolved, pointing out that the error growth in the HWRF simulations was dominated by the error in the low-order wavenumbers. However, Vukicevic et al. (2014) primarily looked at the residual stochastically, rather than as a measure of the changing vortex structure, calculating its mean value and standard deviation from numerous simulations.

While Vukicevic et al. (2014) attempted to describe a new multiscale intensity metric that could be used to evaluate TC intensity forecasts, they also demonstrated a vortex-scale context for evaluating the representativeness of the vortex intensity estimates from simulations and SFMR observations. They showed in their Fig. 1a that the amplitude of the sum of the two low-order wavenumbers (i.e., $0 + 1$) is very highly correlated to the simulated peak 10-m wind speed, and in their Fig. 2 they showed how well that amplitude tracks the simulated peak 10-m wind speed in time throughout the storm's evolution. Examination of their Fig. 2 strongly suggests that the residual between and the sum of wavenumbers 0 and 1 (represented by their term ε) can be treated as stochastic white noise superposed upon the sum of the two low-order wavenumbers. Their Fig. 1b further suggests that the only difference between the observed and model variance in the wind field is the spread of the probability density function (PDF) of this white noise, with the model, in this case a 3-km horizontal resolution Hurricane Weather Research and Forecasting (HWRF) Model[1] simulation, having less spread than observed.

---

[1] Our examination of the stochastic residual for the 1-km horizontal resolution WRF simulation examined in Uhlhorn and Nolan (2012) indicated that the PDF of ε was broader than in HWRF, closer to that observed (not shown), suggesting that different models and resolutions can produce slightly different stochastic residuals. However, in both cases the sum of the low-order wavenumbers was highly correlated to the simulated peak 10-m wind speed as found by Vukicevic et al. (2014).
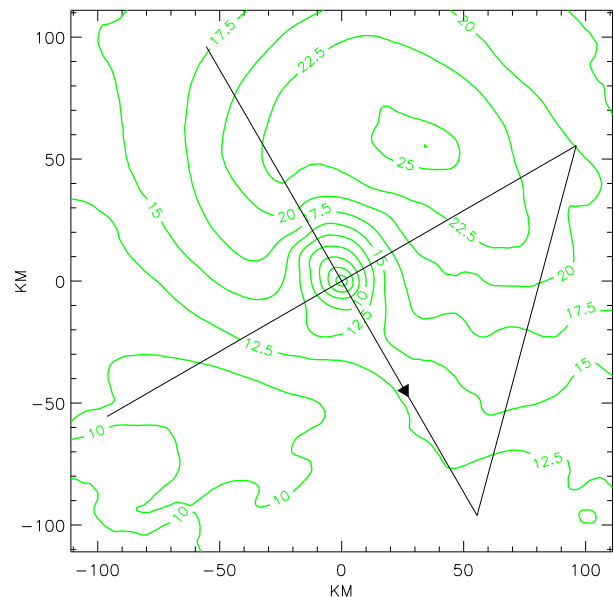

FIG. 1. Typical figure-four flight pattern used during data collection. The illustration is in storm-relative coordinates and the contours representing the storm's Earth-relative wind speed in the illustration are contours of the mean model wind speed from 1800 UTC 28 Aug to 0100 UTC 29 Aug 2010. The contour labels are in m s^{-1}.

This study attempts to extend the work of Vukicevic et al. (2014) by examining how the low-order wavenumbers and the stochastic residual are related to the evolution of the vortex structure throughout a simulation, and how that variability affects an analysis when those values are changing over a typical sampling interval. When the storm is changing hour by hour during an aircraft mission, the analyzed "intensity" may not be well represented by the first two wavenumbers. The question, which then needs to be answered, is "Just how good a representation of the wind speed field is one that includes only wavenumbers 0 and 1, and how is that representation affected when the sampling and wind field varies in time?"

Our purpose is to provide an answer to this question in two specific cases: 1) when the observed storm is in a reasonably steady state and 2) when the observed storm is changing its internal structure significantly over the period of observation. To answer this question, we will need to evaluate the temporal and spatial evolution of the complete surface wind speed fields over a sufficiently long period. Experience analyzing flight-level and Doppler radar wind observations indicates that 8 h is a sufficient time interval to capture vortex evolution. Since such fields are not available from current observing systems, we will use instead, as a nature proxy, wind speed fields generated by the current operational model,
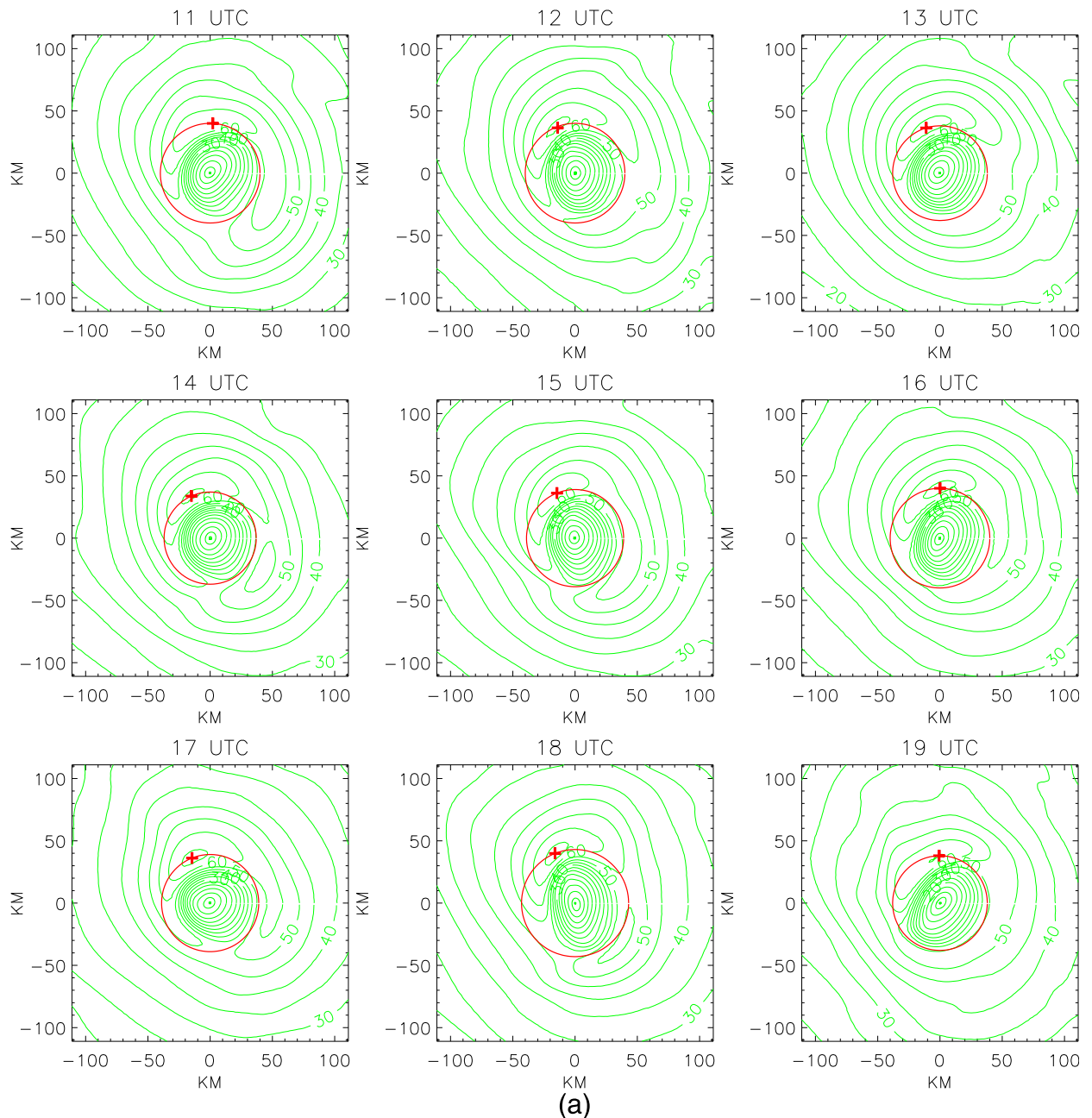
FIG. 2. (a) Contour plots of the model surface (10 m) wind speed field hour by hour for the SS period from 1100 to 1900 UTC 31 Aug 2010. Panels are in storm-relative coordinates and contour labels are in m s^{-1}. The boldface plus sign (+) in each panel indicates the location of the peak wind speed for each hour and the red circle denotes the RMW. (b) Perspective surface plots of the model surface (10 m) wind speed field hour by hour for the SS period from 1100 to 1900 UTC 31 Aug 2010; panels are in storm-relative coordinates and the wind speed (vertical) axis is in m s^{-1}; both of the horizontal axes are from −100 to 100 in increments of 50 km.

HWRF, since it is used by the National Hurricane Center (NHC) as an aid to forecasting. Its purpose for this study is simply to provide credible high-resolution wind speed fields to permit the computation of a large enough set of wavenumber components so that we may determine how effective a field representation containing only the first two wavenumbers can be.

Section 2 describes our methodology. Section 3a will consider the "steady state" (SS) period. The set of wind speed fields depicting this situation is an HWRF simulation of Hurricane Earl on 31 August 2010 between the hours of 1100 and 1900 UTC. Section 3b will address the "non-steady-state" (NSS) period, namely when the storm is altering its internal structure hour by
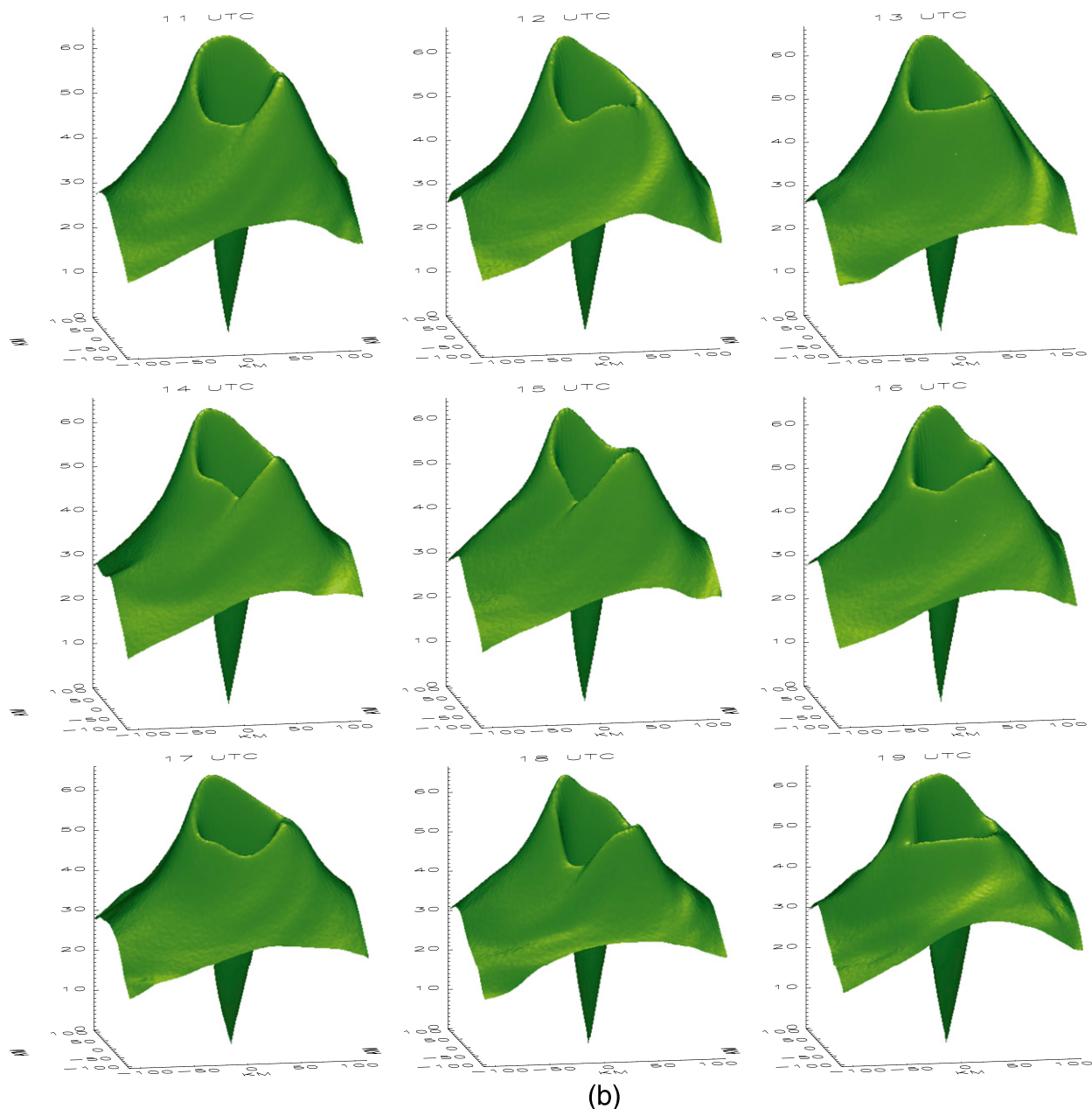
(b)

FIG. 2. (*Continued*)

hour. The set of wind speed fields depicting this situation is from the same HWRF simulation of Hurricane Earl from 1800 UTC 28 August to 0100 UTC 29 August 2010.

2. Data and analysis method

a. Data

Our set of wind speed fields is obtained from a HWRF simulation of Hurricane Earl initialized at 1800 UTC 27 August 2010 [24 h after the simulation described in Chen and Gopalakrishnan (2015)]. The HWRF system was developed at NOAA/National Weather Service/NCEP to address the nation's hurricane forecast problems and became an operational track and intensity guidance tool in 2007. In this work, we used the 2012 version of the operational HWRF system (e.g., Tallapragada et al. 2014; Gopalakrishnan et al. 2012). The model is nonhydrostatic formulated on a rotated latitude–longitude, Arakawa E grid and has a vertical, pressure hybrid (sigma *p*) coordinate centered on the storm. The model is triply nested and configured with a coarse mesh of 27-km horizontal grid spacing covering

about $75° \times 75°$ with two embedded two-way moving meshes (an intermediate 9-km horizontal grid covering about $11° \times 10°$ and a 3-km innermost horizontal mesh covering about $6° \times 5°$). There are 42 hybrid levels with 11 levels below the 850-mb level, the lowest at 10 m (surface). In addition, the operational HWRF system is coupled to a three-dimensional version of the Princeton Ocean Model (POM) modified for hurricane applications over the Atlantic basin. Documentation for the HWRF system is available at the Development Testbed Center (DTC), National Center for Atmospheric Research (NCAR), in Boulder, Colorado (http://www.dtcenter.org/HurrWRF/users/docs/users_guide/HWRF_v3.6a_usersguide.pdf).

Surface wind speed fields on the 3-km innermost mesh at two time periods in the simulation are analyzed: 1) from 1100 to 1900 UTC 31 August 2010 (89–97 h into the simulation) when the storm was a near-steady-state hurricane and 2) from 1800 UTC 28 August to 0100 UTC 29 August 2010 (24–31 h into the simulation) when the simulated storm was beginning its intensification from a tropical storm to a hurricane.

b. Wavenumber field description

The wavenumber K representation of a two-dimensional wind speed field $WS(r, \phi)$ will include all wavenumbers (WVNs) up to and including K, where K ranges from 0 to 5, while a single wavenumber component j of the wind speed field is given by

$$ws_j(r,\phi) = C_j(r)\cos(j\phi) + S_j(r)\sin(j\phi) \qquad (1)$$

$$WVN(0:K) = \sum_{j=0}^{K} ws_j(r,\phi). \qquad (2)$$

Here, (2) defines the complete wavenumber K representation of the field, where r is the radial distance from the origin of the storm-centered polar coordinate system and ϕ is the mathematical azimuth measured counterclockwise from the positive x axis.

For $j = 0$, $\cos(j\phi) = 1$ and $\sin(j\phi) = 0$, so that $S_0(r)$ is arbitrary and may be set to 0, and $C_0(r)$ is the wavenumber 0 wind speed radial profile:

$$C_0(r) = \frac{1}{2\pi} \int_0^{2\pi} WS(r,\phi)\, d\phi. \qquad (3)$$

The radial function associated with the cosine dependence of the jth wavenumber is $C_j(r)$ and $S_j(r)$ is likewise the radial function associated with the corresponding sine dependence. These functions are obtained from the model wind speed field $WS(r, \phi)$, according to

$$C_j(r) = \frac{1}{\pi} \int_0^{2\pi} WS(r,\phi)\cos(j\phi)\, d\phi \quad \text{and} \qquad (4)$$

TABLE 1. Hourly values of RMW, WS_{MAX}, and AZIM for the SS period (1100–1900 UTC 31 Aug).

Time (UTC)	RMW (km)	WS_{MAX} (m s^{-1})	AZIM (°)
1100	40	65	3
1200	40	66	339
1300	38	67	343
1400	37	66	336
1500	39	65	338
1600	40	67	0
1700	39	66	338
1800	43	67	338
1900	38	65	359
Mean	39	65.8	346
AAD	1.3	0.6	9.8

$$S_j(r) = \frac{1}{\pi} \int_0^{2\pi} WS(r,\phi)\sin(j\phi)\, d\phi, \qquad (5)$$

for $1 \le j \le 5$.

c. Analysis method

Three essential storm characteristics are used to determine whether an analyzed low-order wavenumber depiction adequately represents the model snapshot wind speed field:

1) magnitude of the peak wind speed (WS_{MAX}),
2) radius of maximum wind (RMW), and
3) azimuth of the peak wind speed (AZIM).

These are chosen since they bear directly on the location and spatial extent of any storm-related damage.

3. Results

a. Model storm changing slowly with time

Figures 2a and 2b illustrate the model wind speed field for Hurricane Earl on 31 August 2010 between 1100 and 1900 UTC. Perusal of these figures shows clearly that the model storm, albeit not absolutely stationary, is changing only very slowly with time. Note the striking similarity of the individual panels with each other and the presence of a symmetric primary circulation throughout the 8-h SS period. Table 1 shows the RMW with a mean of 39 km and an average absolute deviation (AAD) of 1.3 km, as well as a mean WS_{MAX} of 65.8 m s^{-1} with an AAD of 0.6 m s^{-1}. Finally, Table 1 shows also the mean AZIM of 346° with an AAD of 9.8°.[2]

Figure 3 shows the time mean and AAD of the model wind speed field for all points within a 2° box around the

---

[2] AZIM values listed in Table 1 and all other tables to follow refer to the meteorological azimuth measured in degrees clockwise from north.
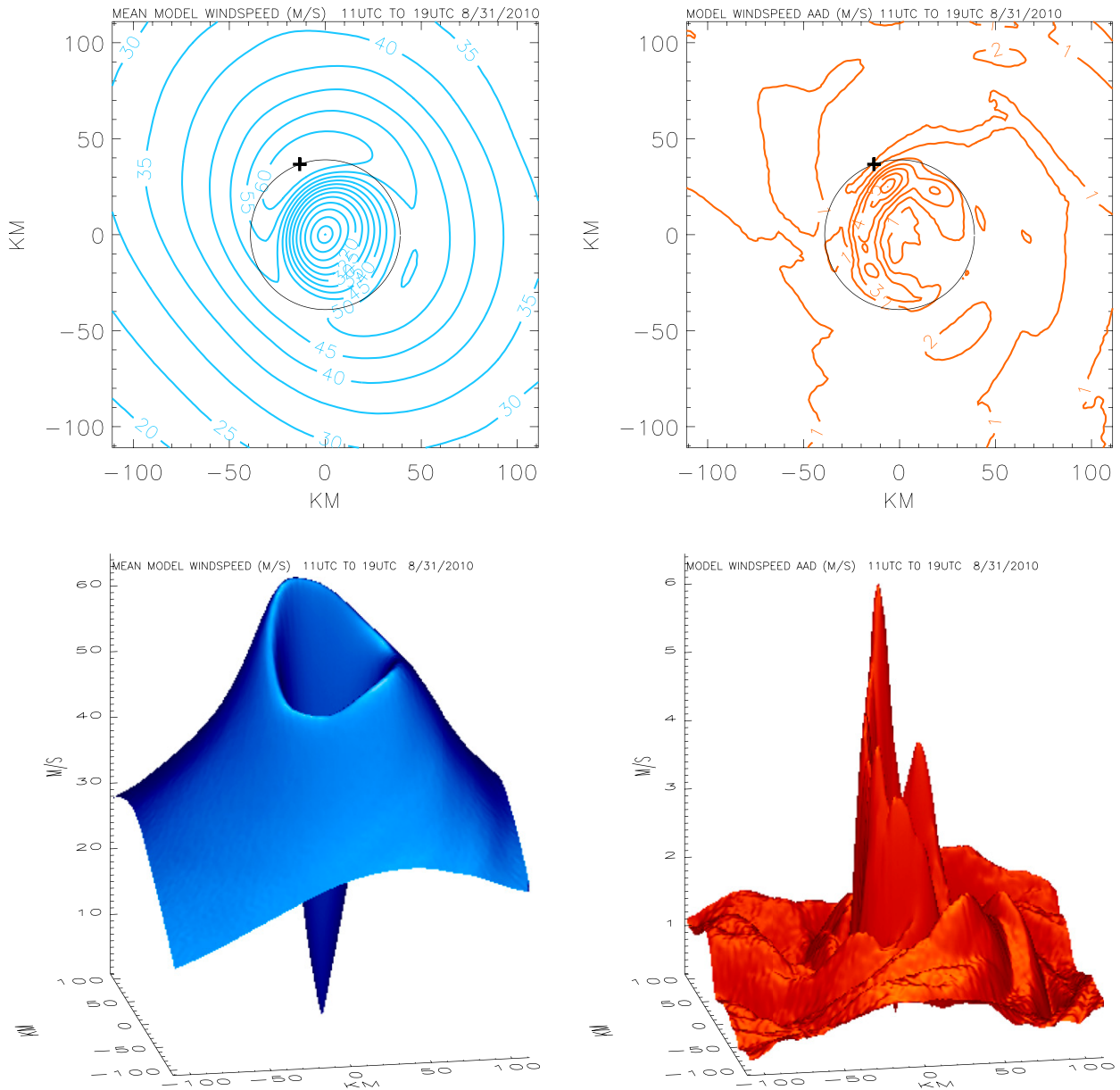
FIG. 3. (top left) The mean model surface (10 m) wind speed contours (m s^{-1}) from 1100 to 1900 UTC 31 Aug 2010; the bold face plus sign (+) indicates the location of the peak wind speed of the mean model field, and the circle shows the RMW for the mean model field. (bottom left) The mean model surface wind speed surface for the SS period. (right) As in (left), but for the AAD of the model surface wind speed field for the same time interval; the vertical axis in the bottom panel is from 0 to 6 in increments of 1 m s^{-1}.

storm center over the 8-h period 1100–1900 UTC 31 August. The top two panels also show the location of the mean model WS_{MAX}. Note the smoothness of the mean surface and its similarity to the 1300 UTC model wind speed surface illustrated in Fig. 2b. The peak mean model wind speed is 65 m s^{-1} and the maximum AAD is 6.5 m s^{-1}, occurring well inside of the RMW (39 km) of the mean model wind speed field, where the wind speed gradient is high.

Figure 4 shows the time mean radial profiles $C_j(r)$ and $S_j(r)$ for wavenumbers 0–5 over the entire SS period and their variation as a function of radial distance (r) from the storm center. For $C_0(r)$, the range of variation does not exceed ± 1.2 m s^{-1} over the entire radial extent of 222 km, while the maximum value of $C_0(r)$ is 54.8 m s^{-1}. The range of $C_1(r)$ is between -9.2 and 4.8 m s^{-1}, while its range of variation at any particular value of r is ± 1.5 m s^{-1}. For $S_1(r)$, the variance is between -0.1 and
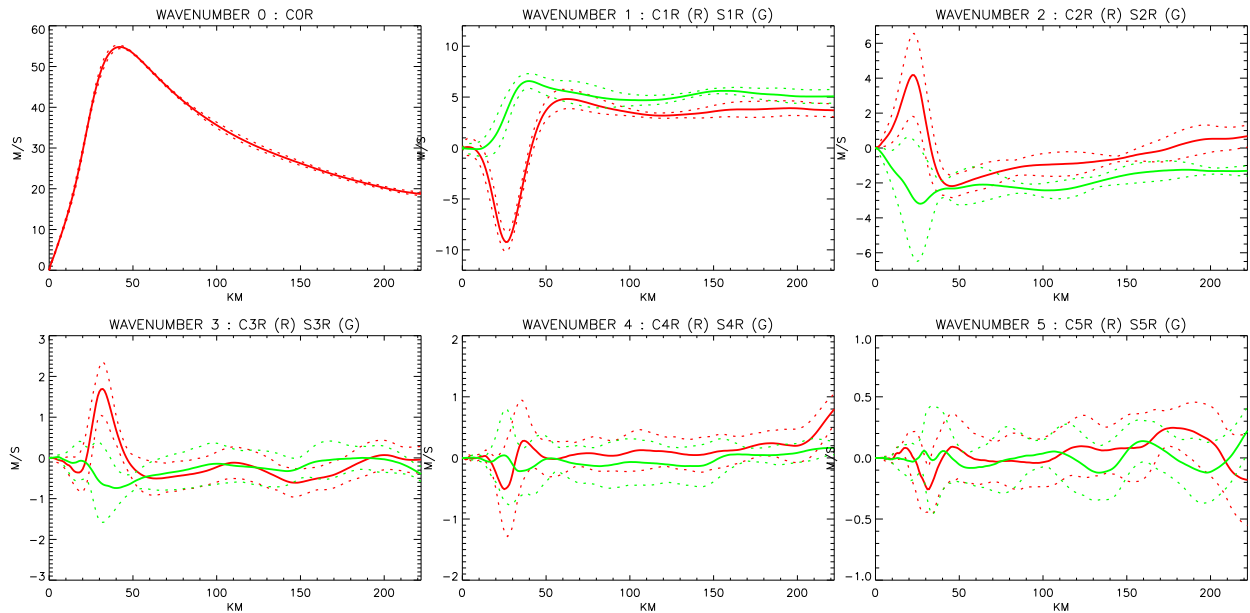
FIG. 4. Time mean cosine (red) and sine (green) amplitude profiles as functions of radial distance (km) from the storm center along with their ranges of variation for (top left to bottom right) each of the first six wavenumbers. The range of variation about a particular mean amplitude profile consists of two dotted lines plotted above and below the profile with values at a given radial distance equal to the mean profile value plus the AAD at that distance for the top line and equal to the mean profile value minus the AAD for the bottom line. These additional dashed lines thus function as ''error bars,'' indicating how much the selected profile can vary throughout the 8-h period and also which radial distances show the greatest variation for that profile. The y axes for each panel are in $\mathrm{m\,s^{-1}}$ and are: wavenumber 0, from 0 to 50 in increments of 10; wave number 1, -10 to 10 in increments of 5; wavenumber 2, -6 to 6 in increments of 2; wavenumber 3, from -3 to 3 in increments of 1; wavenumber 4, from -2 to 2 in increments of 1; and wavenumber 5, from -1 to 1 in increments of 0.5. All the x axes are in 0 to 200 in increments of 50 km.

$6.6\,\mathrm{m\,s^{-1}}$ and its range of variation is $\pm 1.8\,\mathrm{m\,s^{-1}}$, as illustrated in the second panel of Fig. 4. Table 2 summarizes the results for the first six wavenumbers.

To discuss the effectiveness of the wavenumber representations for a particular snapshot, we select the model wind speed field at 1300 UTC since this instance of the model field appears to be the smoothest in appearance judging from the panels in Figs. 2a and 2b. Figure 5 shows the representations of the model wind speed field at 1300 UTC when we include only wavenumbers 0:1, 0:2, and 0:3, as well as the complete model field. Here, we see that the wavenumber (0:1) certainly captures the essential features of the model field. Although the peak wind speed ($62\,\mathrm{m\,s^{-1}}$) is 7% too low and the RMW (40 km) is 5% too large, the azimuth of the peak wind is correct and the general pattern and placement of the isotachs are quite good. The surface graphics more strikingly show the contribution of each wavenumber to WS_{MAX} and AZIM, as each wavenumber is included in the field representation and they clearly establish how quickly the sequence of wavenumber representations converges to the actual model wind speed field in this SS period. Figure 5 clearly shows that wavenumbers 2 and 3 account for nearly all of the

shortcomings of the wavenumber (0:1) portrayal. Table 3 gives the improvement in the evaluation of WS_{MAX}, RMW, and AZIM as we increase the wavenumbers present in the successive wind speed field representations.

In a real sense, provided that the model wind field is representative of the real wind field, these results give a ''best case'' scenario indicating what we can expect from any analysis of the surface wind speed based on observations collected during an actual storm that attained a reasonably ''steady state.'' They indicate that we can expect to determine the characteristics of the wind

TABLE 2. Magnitudes and range of the radial function associated with the cosine dependence of the jth wavenumber $C_j(r)$ and the corresponding sine dependence $S_j(r)$, where $j = 0$–5, for the 8 h of the SS period (1100–1900 UTC 31 Aug).

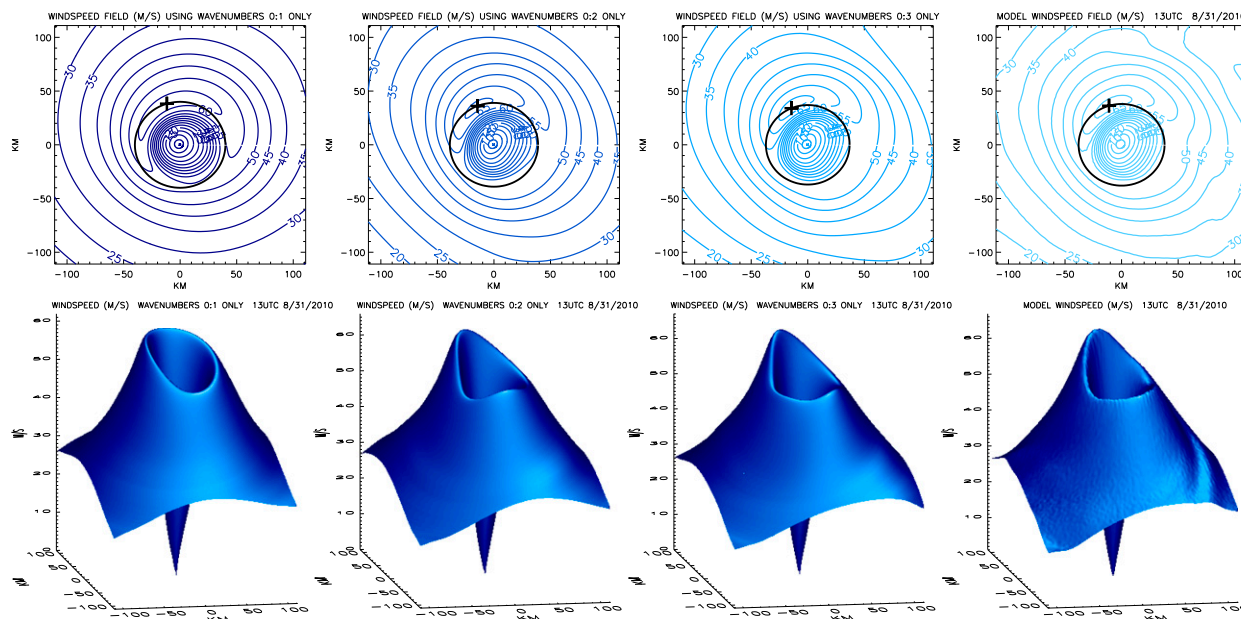| j	$C_{j\mathrm{min}}$ $(\mathrm{m\,s^{-1}})$	$C_{j\mathrm{max}}$ $(\mathrm{m\,s^{-1}})$	C_j range $(\mathrm{m\,s^{-1}})$	$S_{j\mathrm{min}}$ $(\mathrm{m\,s^{-1}})$	$S_{j\mathrm{max}}$ $(\mathrm{m\,s^{-1}})$	S_j range $(\mathrm{m\,s^{-1}})$
0	0	54.8	± 1.2			
1	-9.23	4.8	± 1.5	-0.11	6.57	± 1.8
2	-2.18	4.2	± 2.4	-3.19	0	± 3.4
3	-0.61	1.7	± 0.7	-0.74	0.02	± 1
4	-0.51	0.8	± 0.9	-0.21	0.16	± 0.8
5	-0.26	0.25	± 0.4	-0.12	0.22	± 0.4

FIG. 5. Representations of the model surface wind speed field containing (left to right) only wavenumbers (0:1), (0:2), and (0:3 and compared with (extreme right) the actual model wind speed field at 1300 UTC 31 Aug 2010, both as (top) contour and (bottom) perspective surface plots. In each of the contour plot panels, the position of the peak wind as well as the RMW is depicted via the boldface plus sign (+) and the black circle, respectively. The y and x axes in the top plots are from -100 to 100 in increments of $50\,\mathrm{m\,s^{-1}}$. The vertical axes in the bottom plots are from 0 to 60 in increments of $10\,\mathrm{m\,s^{-1}}$ and the horizontal axes are as in Fig. 2.

speed field fairly accurately from an analysis containing only wavenumbers 0, 1, and 2.

The model and analysis wind speed field primary circulations are considered symmetric if a symmetry index, defined as the ratio of $(\mathrm{WS_{MAX}} - \mathrm{WVN0})$ to WVN0 calculated at the RMW, is <0.25; otherwise, they are considered asymmetric. This symmetry index is very similar to the multiscale intensity (MSI) metric for evaluating tropical cyclone (TC) intensity forecasts proposed by Vukicevic et al. (2014).

Figure 6 depicts a comparison of simulated versus the "best track" intensity and radius of maximum wind from the extended best-track dataset.[3] Examination of the best-track intensity and RMW in Figs. 6b and 6c, respectively, suggests that this simulation's representation of these variables is comparable to that of Chen and Gopalakrishnan (2015), particularly after the NSS period. It captures the intensification after the NSS period well. Figure 6b indicates a slight overestimate of $\mathrm{WS_{MAX}}$ during the SS period; however, Landsea and Franklin (2013) found that the uncertainty of the best-track peak intensity is roughly 10%. Thus, the simulation is within that uncertainty.

Figure 6a depicts the time series of the symmetry index for the SS period, showing that this ratio remains <0.25 throughout the 8-h period. Such low values of this ratio indicate the primary circulation is relatively symmetric, and the lack of change in this ratio over the 8 h suggests a relatively steady state to the wind speed field. Figure 6a suggests that the period of asymmetry extended from 6 h into simulation until hour 66 (1200 UTC 30 August 2010), with increases from 0.5 to >1.0 during the early portion of the NSS period (hours 25–29, 1900–2300 UTC 28 August 2010), and then decreases to values between 0.3 and 0.5 from hour 31 to 60 as the primary circulation becomes more symmetric. The impacts of these dramatic changes in the symmetry on the wind speed field analysis are discussed in the next section.

TABLE 3. Values of $\mathrm{WS_{MAX}}$, RMW, and AZIM as the number of wavenumbers present in the successive wind speed field representations for 1300 UTC 31 Aug. The "truth" from the model is also listed.

Wavenumbers	$\mathrm{WS_{MAX}}$ (m s^{-1})	RMW (km)	AZIM (°)
0:1	62	40	107
0:2	66	39	112
0:3	67	37	113
0:4	67	38	106
0:5	67	38	104
Model	67	38	107

---

[3] The extended best-track dataset is available online (http://rammb.cira.colostate.edu/research/tropical_cyclones/tc_extended_best_track_dataset/).
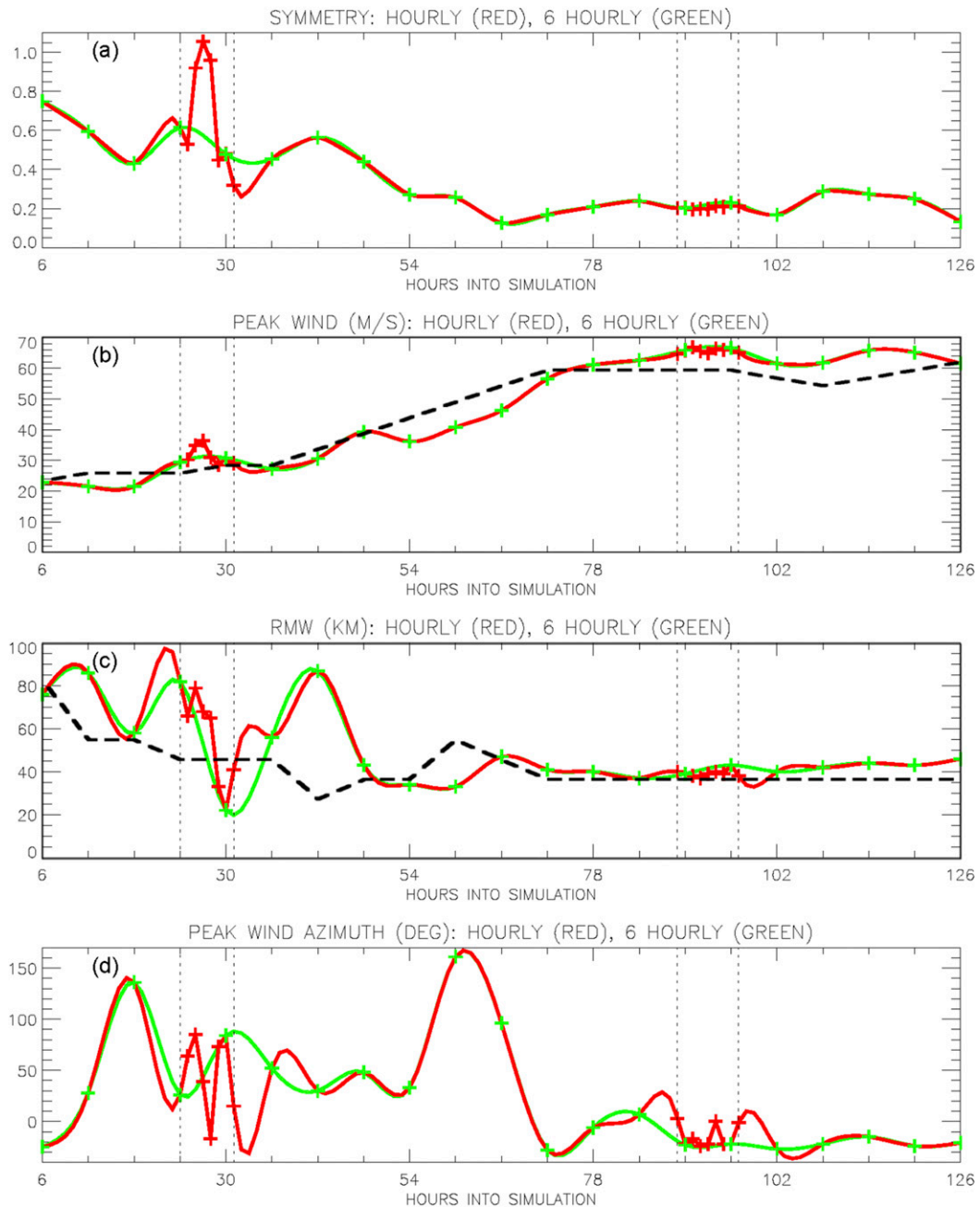
FIG. 6. Time series of the (a) symmetry index, (b) WS_{MAX}, (c) RMW, and (d) AZIM for each 6-h snapshot over the complete 126-h model simulation beginning at hour 6 and ending at hour 126 (green line), and with addition of the 1-h snapshots over the SS and NSS periods (red line). The thick dashed lines in (b) and (c) denote the best-track intensity and RMW, respectively. Vertical dotted lines denote the SS and NSS periods within the 126-h simulation.

b. Model storm changing rapidly with time

Figures 7a,b show the evolution of the surface (10 m) wind speed field produced by the model hour by hour from 1800 UTC 28 August to 0100 UTC 29 August 2010. Note the striking dissimilarity of the individual panels with each other and the asymmetry of the primary

circulation throughout the 7-h NSS period except for the last few hours. The position of WS_{MAX} varies considerably with time, although the value of WS_{MAX} does not vary much over the interval, as indicated in Table 4.

The Table 4 also contains the mean RMW, WS_{MAX}, and AZIM and their AADs. The AADs for this NSS time interval are much larger than the corresponding values
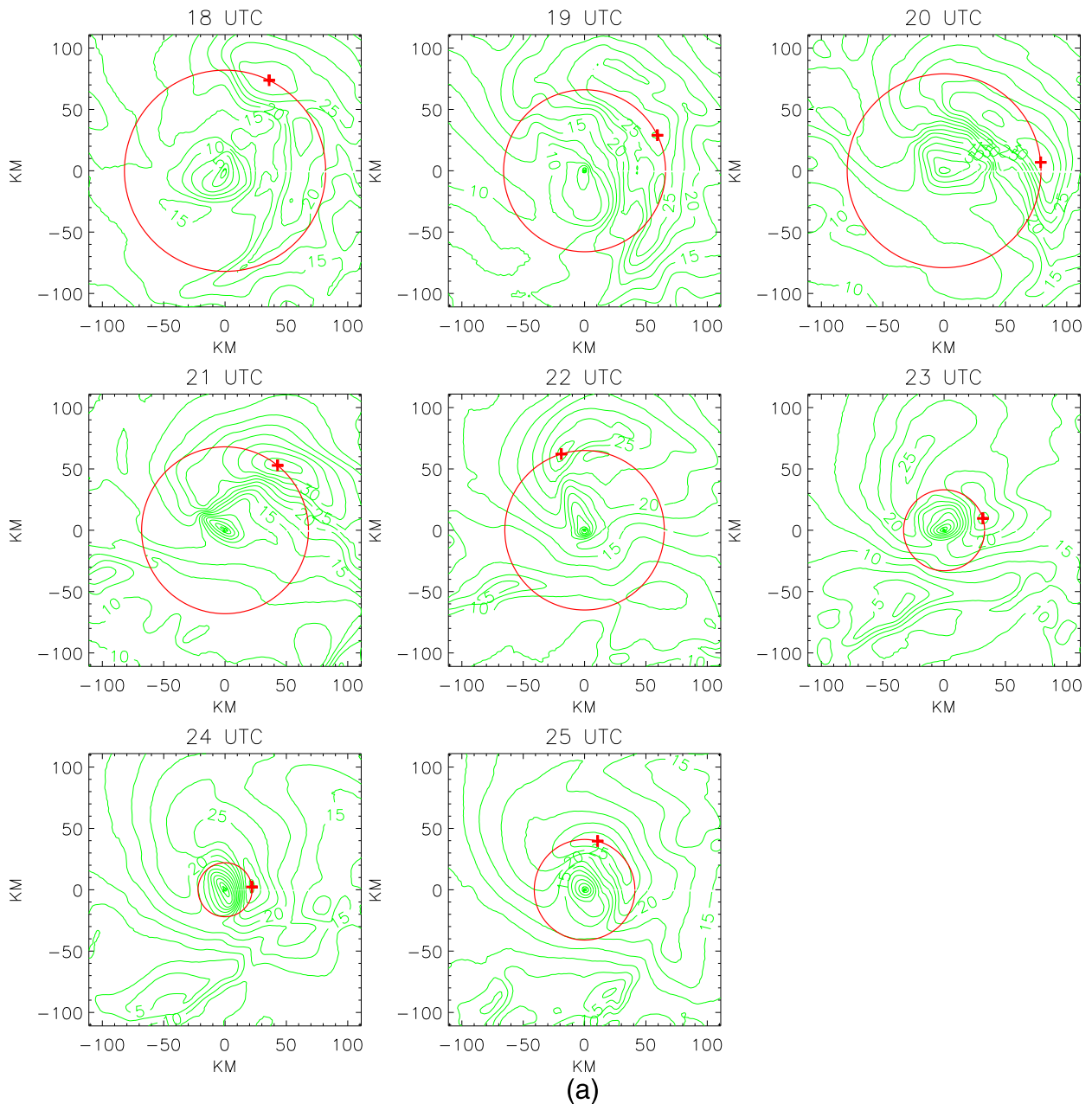
FIG. 7. As in Fig. 2, but for the NSS period from (top left to bottom right) 1800 UTC 28 Aug to 0100 UTC 29 Aug 2010. Note that the vertical axes in the perspective surface plots vary; the top row is from (left to right) 0 to 25+, 0 to 30, and 0 to 30+ in increments of 5 m s^{-1}; and in the bottom row from (left to right) 0 to 30+, and 0 to 25+ in increments of 5 m s^{-1}.

listed in Table 1 for the SS period. Table 4 shows the smallest AAD for WS$_{MAX}$ and the largest for AZIM. The surface graphics (Fig. 7b) show that from 1800 to 2100 UTC, the primary circulation is very asymmetric.

Figure 8 illustrates the mean and the AAD of the model wind speed field over the 7-h period for all points within a 2° box around the storm center for the NSS period. The peak WS$_{MAX}$ is 26 m s^{-1} and the maximum AAD is 6.1 m s^{-1}. The bottom panel in Fig.8 shows the

mean model 10-m wind speed surface for the NSS period. The right-hand column shows the AAD of the model field for the entire 7-h period. Figure 8 shows that the maximum AAD (6.1 m s^{-1}) occurs well inside the RMW, but large values (>4.5 m s^{-1}) are evident throughout the displayed region, in marked contrast to the corresponding panel in Fig. 3 for the SS period. Also, the mean model RMW (65 km), WS$_{MAX}$ (26 m s^{-1}), and AZIM (58°) all differ from the mean values listed in
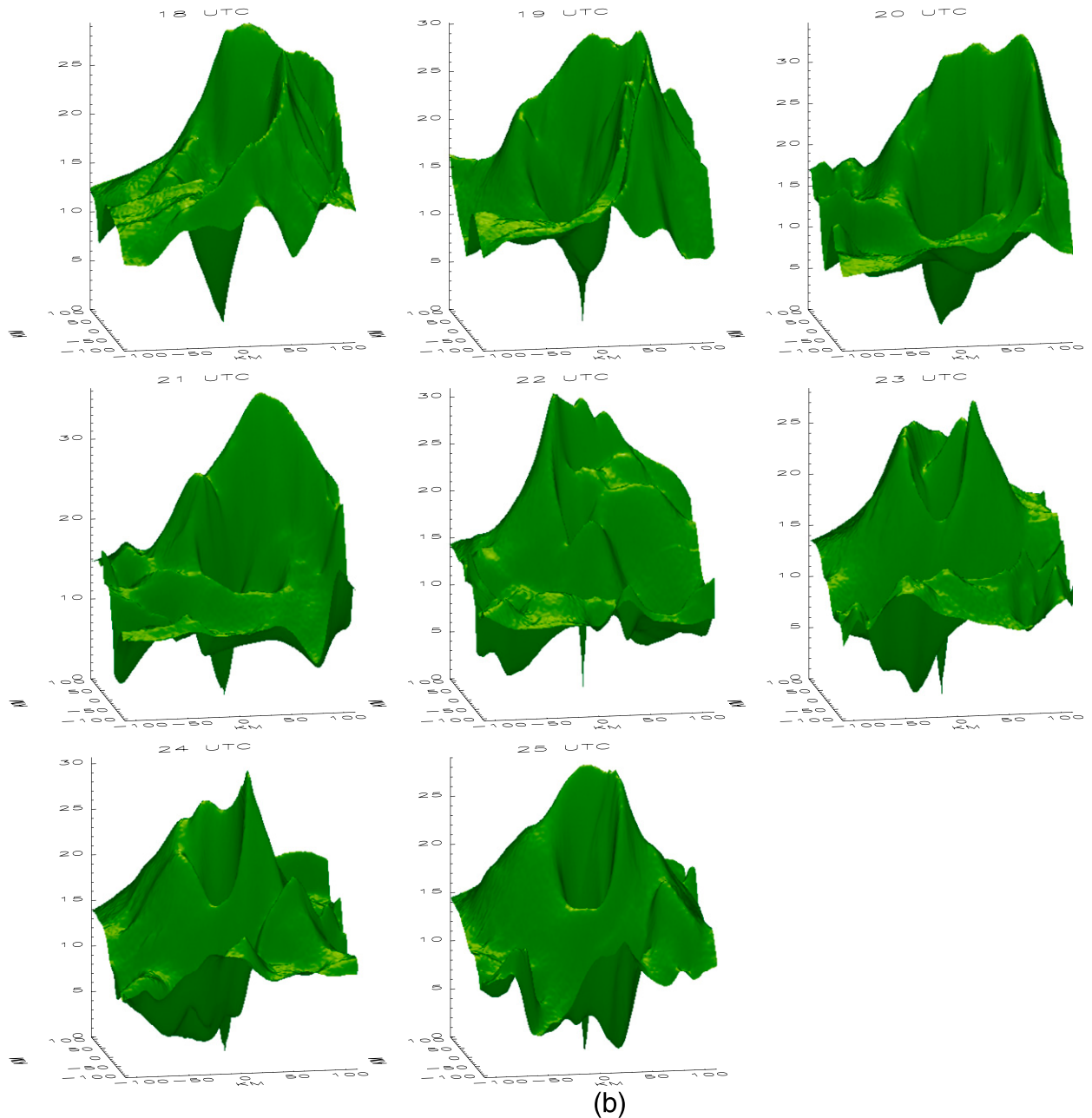
(b)

FIG. 7. (*Continued*)

Table 4. The differences, (8 km, 5 m s^{-1}, and 12°) are within the AADs listed in Table 4 for the RMW and AZIM but for WS$_{MAX}$ the difference is more than twice the AAD listed in Table 4, although less than the maximum model wind speed AAD of 6 m s^{-1}. It should be noted that the values in Table 4 represent the mean of the maximum wind speed and its location, whereas Fig. 8 shows the maximum (and its location) extracted from the mean wind field (i.e., the mean of the maxima versus the maximum of the mean).

Figure 9 shows the mean radial profiles $C_j(r)$ and $S_j(r)$ for wavenumbers 0–5 and their ranges of variation. Table 5 summarizes the results depicted there for the NSS time interval from 1800 UTC 28 August to 0100 UTC 29 August 2010. Comparing Fig. 9 with Fig. 4 for each of the mean wavenumber profiles illustrated, the corresponding ranges of variation and position of the largest variation are, respectively, smaller and closer to the storm center for the SS period than they are for the NSS period. The amplitude

TABLE 4. Hourly values of RMW, WS_{MAX}, and AZIM for the NSS period (1800 UTC 28 Aug–0100 UTC 29 Aug).

Time (UTC)	RMW (km)	WS_{MAX} (m s^{-1})	AZIM (°)
1800	82	29	26
1900	66	30	64
2000	79	35	85
2100	68	36	39
2200	65	31	343
2300	33	28	73
0000	22	31	84
0100	41	29	15
Mean	57	31.3	46
AAD	18.8	2.2	30.4

of wavenumber 2 during the SS period (Fig. 4) is a maximum typically just inside the RMW where the gradient of the wavenumber 0 radial wind profile is greatest. Outside the RMW the wavenumber 2 amplitude is much smaller, suggesting that in the SS period the wavenumber 2 structures are primarily modulating the steepness of the gradient inside the RMW, not WS_{MAX}, whereas during the NSS period (Fig. 9) the wavenumber 2 amplitude is high inside the RMW and also at radii > 125 km. The inner maximum is likely a result of similar features to those in the SS period, but the outer maximum is in the portion of the vortex where rainbands are much more common, which possibly explains the increase.

Examination of Fig. 6a shows that the symmetry index averages ~0.7 for the NSS period, indicating an asymmetric primary circulation, while it is <0.25 for the SS period, indicating a symmetric primary circulation. Comparison of Fig. 6a with Figs. 6b–d also indicates that WS_{MAX} started increasing steadily from the end of the NSS period at hour 31 (0100 UTC 29 August 2010) until the end of the SS period at hour 97, while the RMW and the symmetry index fluctuated dramatically until hour 54 (0000 UTC 30 August 2010). Hence, WS_{MAX} began increasing while the vortex was still asymmetric, the RMW was fluctuating between 30 and 80 km, and the AZIM was fluctuating between 90° and 330°. It also appears that WS_{MAX} began to intensify fairly rapidly as the RMW and symmetry index became relatively steady, suggesting that while WS_{MAX} starts increasing before the vortex becomes more symmetric, it increases faster once the vortex is more symmetric.

Miyamoto and Takemi (2013) developed a metric (γ) similar to our symmetry index to define what they call the "axisymmetricity" of the simulated storm. They defined γ for any variable in the model field as the ratio of the squared wavenumber 0 component to the sum of squared wavenumber 0 and asymmetric components averaged over a cylinder 100 km in radius and from 1.5- to 12-km

altitude. When the circulation has no asymmetries, $\gamma = 1$.[4] They applied it to potential vorticity over the simulation and showed γ varies from 0.1 as the vortex was developing and increased to >0.8 as the vortex rapidly intensified. Much as we noted in our results, their γ fluctuated considerably early in the simulation and stabilized near 0.9 after the rapid intensification ended.

Since the model wind speed field changes so dramatically during the NSS period, and to emphasize the importance of a symmetric primary circulation to the low-order wavenumber analyses, we will depict how the individual representations compare to the actual model wind speed field as we include each higher wavenumber for *two* instances of the model field, namely 1800 UTC 28 August 2010, which is at the beginning of our selected time interval, and 0000 UTC 29 August 2010.

Figure 10 illustrates both as contour and surface plots of the wavenumber (0:1), (0:2), and (0:3) representations as well as the actual model wind speed field at 1800 UTC 28 August 2010. The surface panels clearly establish how poorly the sequence of wavenumber representations converges to the actual model wind speed field during this NSS period. The wavenumber (0:1) representation yields a WS_{MAX} of 25 m s^{-1} with an RMW of 70 km and with an AZIM of 66°. The corresponding values for the model wind speed field at this time are 30 m s^{-1}, 82 km, and 28°. The value of WS_{MAX} is too small by 17%. The RMW is too low by 15% and AZIM differs by 38°.

Including wavenumber 2 improves WS_{MAX}, differing only by 3 m s^{-1} from the model value. The RMW, however, is 24% too large. There is a modest improvement in AZIM, differing from the model value by 13°. The wavenumber (0:3) representation gets closer to the truth, giving a WS_{MAX} of 28 m s^{-1}, and an RMW of 86 km and AZIM of 33°. The surface graphics show clearly how much of the model wind speed detail is lost if only the first two wavenumbers are included. The wavenumber (0:1) representation is clearly only able to depict the model wind speed field in a very crude fashion.

Table 6 gives the improvement in the evaluation of WS_{MAX}, RMW, and AZIM as we increase the number of wavenumbers present in the successive wind speed field representations. Table 6 shows that for wavenumbers 2 and 3, the differences between the characteristics for each increasing wavenumber of the model field are roughly twice as large as the corresponding differences during the SS period (Table 3) even though the NSS model field is much weaker than during the SS

---

[4] It should be noted that our symmetry index (lower = more symmetric) is opposite to that of Miyamoto and Takemi (higher = more symmetric).
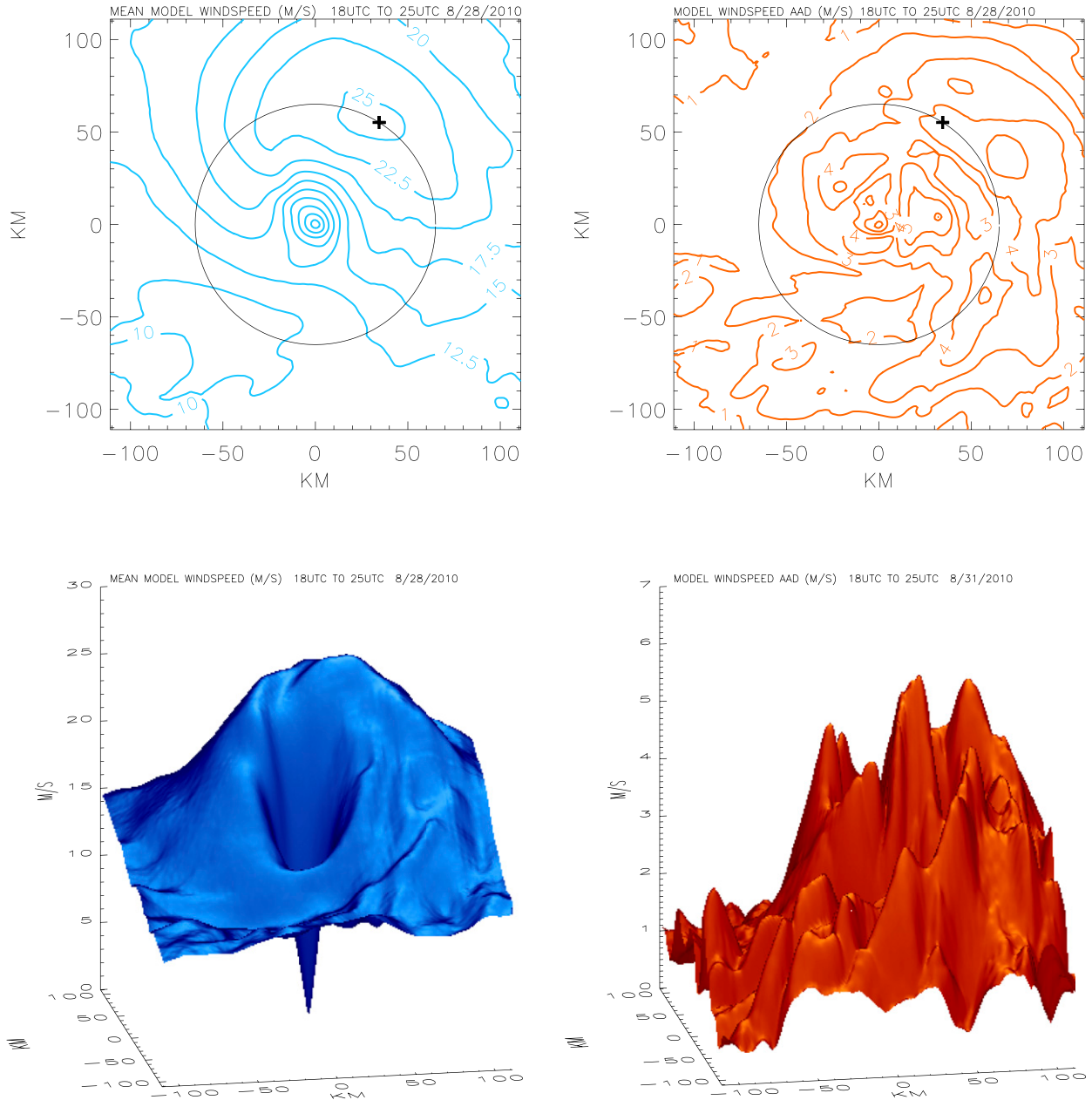
FIG. 8. As in Fig. 3, but from 1800 UTC 28 Aug to 0100 UTC 29 Aug 2010.

period. The convergence of the model wind speed field characteristics is much worse during the NSS period.

Figure 11 illustrates the wavenumber (0:1), (0:2), and (0:3) representations and the actual model wind speed field at 0000 UTC 29 August 2010 in a manner identical to Fig. 10. Comparison of the analyses in Figs. 10 and 11 depicts a much-improved representation of the low-order wavenumbers as a result of the more symmetric primary circulation present in the storm's surface wind speed field at the later time. Figure 6 and Table 7 show that as the symmetry increased in the primary circulation,

the ability of the low-order wavenumber representations to better capture all three of the essential storm characteristics improved.

4. Discussion

a. Representativeness of low-order wavenumber analyses

There are three properties of the model wind speed field that indicate how well the first few wavenumber representations will describe the model field:
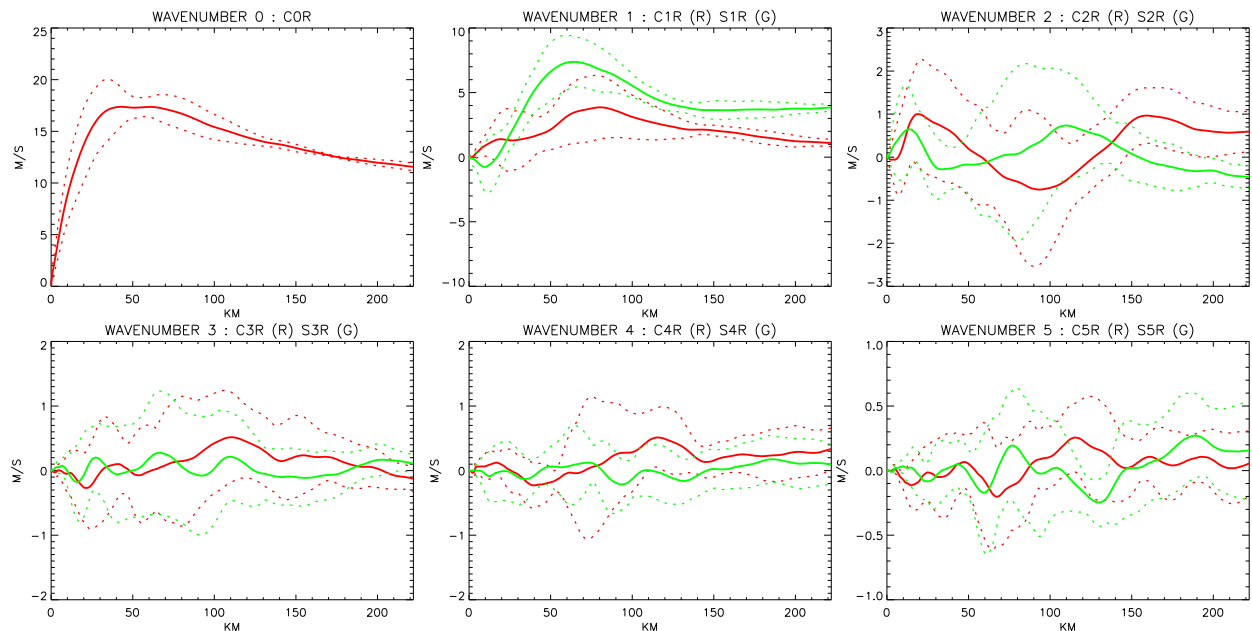
FIG. 9. As in Fig. 4, but for the 7-h period from 1800 UTC 28 Aug to 0100 UTC 29 Aug 2010.

1) the rate at which the WS$_{MAX}$, RMAX, and AZIM are changing hour by hour;
2) the degree of symmetry of the model primary circulation; and
3) how well the hourly model wind speed fields resemble the mean model wind speed field over an analysis interval.

During the NSS period we find a dichotomy in the rate of convergence of the wavenumber representation sequence to the model wind speed field. The main property that most likely accounts for the poor convergence is the rapidly changing and asymmetric primary circulation. In this instance, the wavenumber (0:1) representation is not capable of capturing WS$_{MAX}$, RMAX, and AZIM.

Throughout the NSS period, the temporal mean model wind speed does not resemble any of the hourly instances of the model field and also that at radii beyond the RMW the ranges of variations (in time) of the amplitude of all the wavenumbers are greater for the NSS period than for the SS period (Fig. 9). In an actual data collection scenario, it takes several hours to collect the data from a single figure-four flight pattern, during which time the storm wind field may be changing. Moreover, although the four radial legs of the flight pattern are sufficient to determine the radial profiles for wavenumbers 0 and 1 if they were the only wavenumbers present in the wind speed field, it must be kept in mind that even wavenumbers can alias onto wavenumber 0 and odd wavenumbers can alias onto

wavenumber 1 because only one flight pattern is used during the data collection process. Even in the best of circumstances where all wavenumbers greater than 1 were negligible, there is still the question: "To which time do the radial profiles obtained from the data collection apply?" These concerns, namely the effect of the aliasing of higher-order wavenumbers onto wavenumbers 0 and 1 and the practical requirement that the wind speed data be obtained over a time interval of several hours, need further investigation and quantification.

b. An observing system sensitivity experiment

We can shed some light on the consequences of the fact that the wind speed data are collected over a substantial time interval using an observing system sensitivity experiment similar to that employed by Uhlhorn

TABLE 5. Magnitudes and range of the radial function associated with the cosine dependence of the jth wavenumber $C_j(r)$ and the corresponding sine dependence $S_j(r)$, where $j = 0$–5, for the 7 h of the NSS period (1800 UTC 28 Aug–0100 UTC 29 Aug).

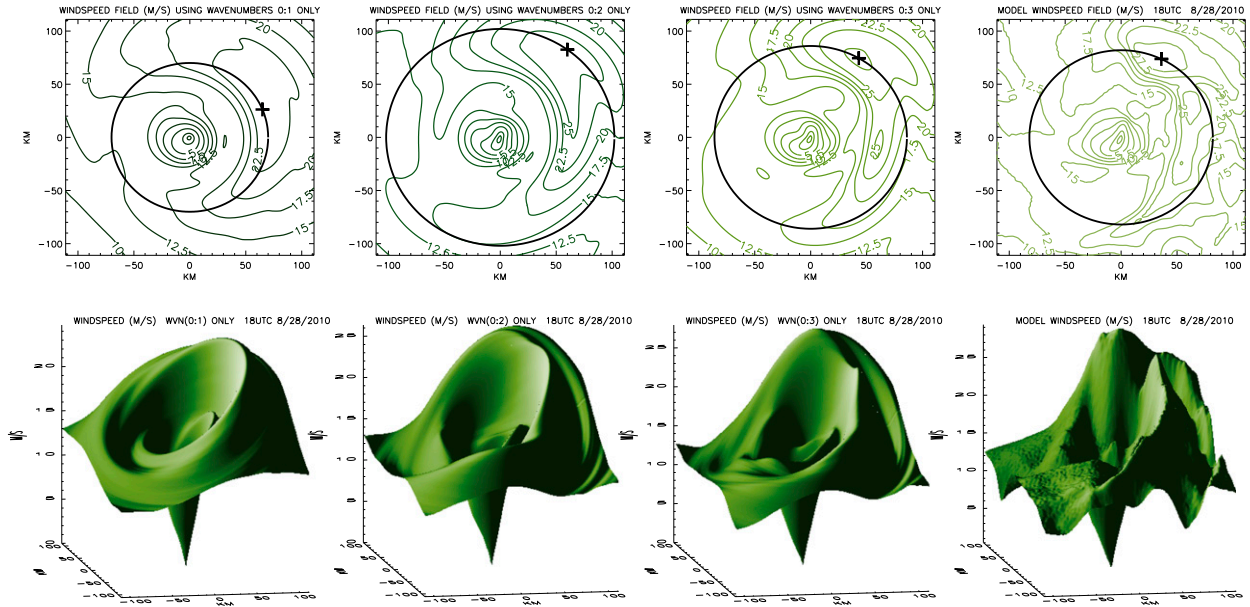| j	C_{jmin} (m s^{-1})	C_{jmax} (m s^{-1})	C_j range (m s^{-1})	S_{jmin} (m s^{-1})	S_{jmax} (m s^{-1})	S_j range (m s^{-1})
0	0	17.37	±3.56			
1	−0.02	3.85	±2.53	−0.76	7.37	±2.28
2	−0.75	1.00	±1.80	−0.46	0.74	±2.04
3	−0.27	0.52	±1.00	−0.18	0.28	±0.96
4	−0.23	0.51	±1.10	−0.21	0.18	±0.61
5	−0.20	0.26	±0.46	−0.25	0.27	±0.50

FIG. 10. As in Fig. 5, but at 1800 UTC 28 Aug 2010. The vertical axis in the bottom plots are from (left to right) 0 to 20+, 0 to 25+, 0 to 25+, and 0 to 20+ in increments of 10 m s^{-1}; and the horizontal axes are as in Fig. 2.

and Nolan (2012). Consider a flight pattern where the four legs extend in the northeast, northwest, southwest, and southeast directions. There are four different figure-four patterns that can be formed from these four radial legs, depending on which leg is chosen as the first inbound leg (e.g., Fig. 12). In the SS period, there are nine hourly model wind speed snapshots spanning 8 h. For the purposes of this exercise the legs will be chosen to be 222 km in length and we assume that the plane requires the total 8 h to collect the observations[5] along the four radial legs. Figure 13a shows the four wind speed plots as a function of time for each of the four potential figure-four flight patterns for the SS period, each with a different inbound leg. Figure 14 shows the wind speed radial profiles obtained from each of the four legs for each of the four different flight patterns. If the storm were truly in steady state over the 8-h period, then the four panels in Fig. 14, apart from a cyclic permutation of the colors, would be identical and it would make no difference in which order the legs were traversed. Figure 14 shows that the four profile panels, though quite similar, are not identical and reflect some time dependence in the

wind speed field. For each flight pattern, the four wind speed radial profiles will generate the radial basis functions for an analysis of the wind speed field containing only wavenumbers 0 and 1 using only the data collected from that pattern (see the appendix). Figure 15 shows the four resulting analyses.

Table 8 shows the principal storm characteristics obtained from each of the four data collection patterns. For comparison, Table 8 also shows the principal storm characteristics obtained from the wavenumber (0:1) projection of the mean model wind speed field for the SS period. Table 8 shows very good agreement among all of the values obtained for WS$_{MAX}$, and fairly good agreement among the values for the RMW, similar to the results found by Uhlhorn and Nolan (2012). AZIM, however, remains quite variable in a range from 313° to 9°, or a range of 56°. The relatively good agreement

---

[5] The time interval was chosen for convenience, recognizing that the typical length of a reconnaissance figure-four flight pattern is approximately 2.5 h. Substantial temporal changes in the wind speed field can occur on time scales shorter than that of a typical figure-four pattern (e.g., Fig. 6), and so we believe our longer simulated figure fours are reasonable.

TABLE 6. Values of WS$_{MAX}$, RMW, and AZIM as the number of wavenumbers present in the successive wind speed field representations is increased at the beginning of the NSS period (1800 UTC 28 Aug). The truth from the model is also listed.

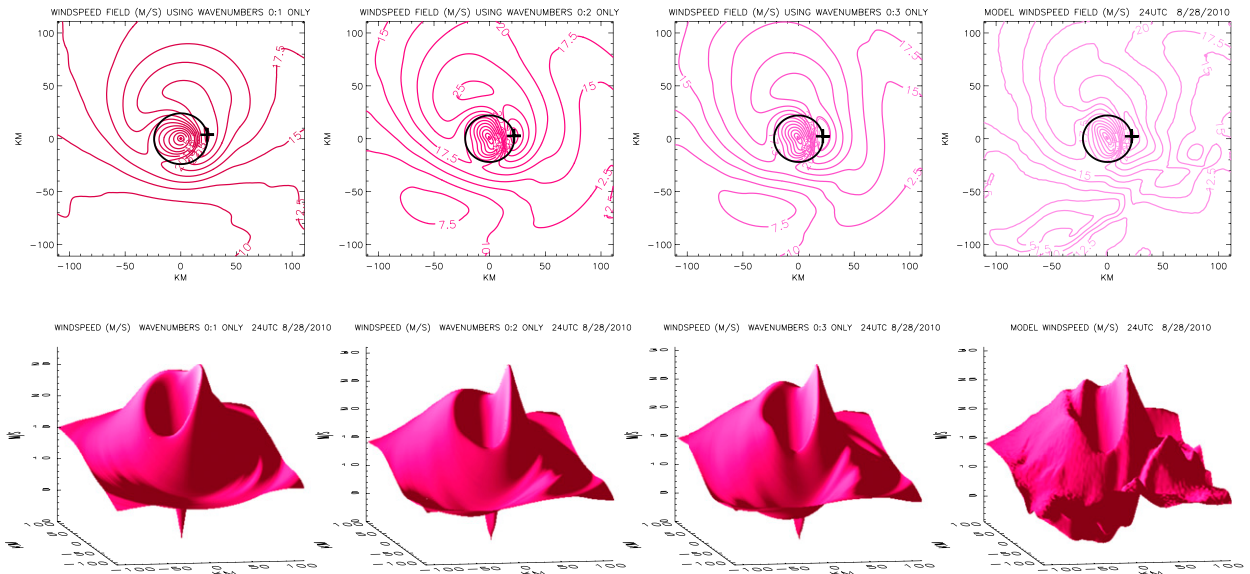| Wavenumbers	WS$_{MAX}$ (m s^{-1})	RMW (km)	AZIM (°)
0:1	25	70	66
0:2	26	102	41
0:3	28	86	33
0:4	28	88	30
0:5	29	87	28
Model	30	82	28

FIG. 11. As in Fig. 5, but at 0000 UTC 29 Aug 2010. The vertical axis in the bottom plots are from (left to right) 0 to 25+, 0 to 30+, 0 to 30+, and 0 to 30+ in increments of 10 m s^{-1}; and the horizontal axes are as in Fig. 2.

between the principal characteristics from the individual patterns and those from the mean model wind speed field over the SS period suggests that, when the vortex is symmetric, aliasing of higher-order wavenumbers on wavenumbers 0 and 1 is not a major issue, and the low-order wavenumber analyses will be very representative.

Next, we consider the same questions for the NSS period. We will use the same four potential flight patterns illustrated in Fig. 12. In this example, however, we use eight hourly model wind speed snapshots spanning 7 h of data collection time. As in the SS period we will assume here that the data collection process requires the full 7 h to fly the pattern.[6] Figure 13b shows the four wind speed plots as a function of time for each of the four potential figure-four flight patterns for the NSS period, each with a different inbound leg. Figure 16 shows the four sets of wind speed profiles as a function of the distance from the center for each of the four different flight patterns. We see from Fig. 16 that the four wind speed profile panels differ significantly from each other as a result of the substantial time dependence of the evolving wind field of the storm. For each flight pattern the four wind speed radial profiles will generate the radial basis functions for the analysis of the wind speed field using only the data collected from that flight pattern. The four resulting analyses are illustrated in Fig. 17, and Table 9 gives the principal

storm characteristics obtained from each of the four data collection patterns as well as that obtained from the wavenumber (0:1) projection of the mean model wind speed field over the 7 h for the NSS period shown in Fig. 8.

Examination of Table 9 shows that WS$_{MAX}$ is in cursory agreement, while RMW and AZIM are clearly not. This is completely different behavior than that shown in the SS example. There is very little resemblance of the wind speed analyses among the four different flight patterns to those obtained from the wavenumber 0 and 1 projection of the mean model field illustrated in Fig. 17, suggesting that, when the storm is asymmetric and varying rapidly in time, the higher-order wavenumbers can significantly be aliased on the low-order wavenumber analyses resulting in an unrepresentative analysis. This aliasing will be manifest in different ways depending on the sampling period, and our choice of 7 h for the sampling duration in our NSS example may not fully represent the magnitude of the aliasing.

TABLE 7. As in Table 6, but for near the end of the NSS period (0000 UTC 29 Aug).

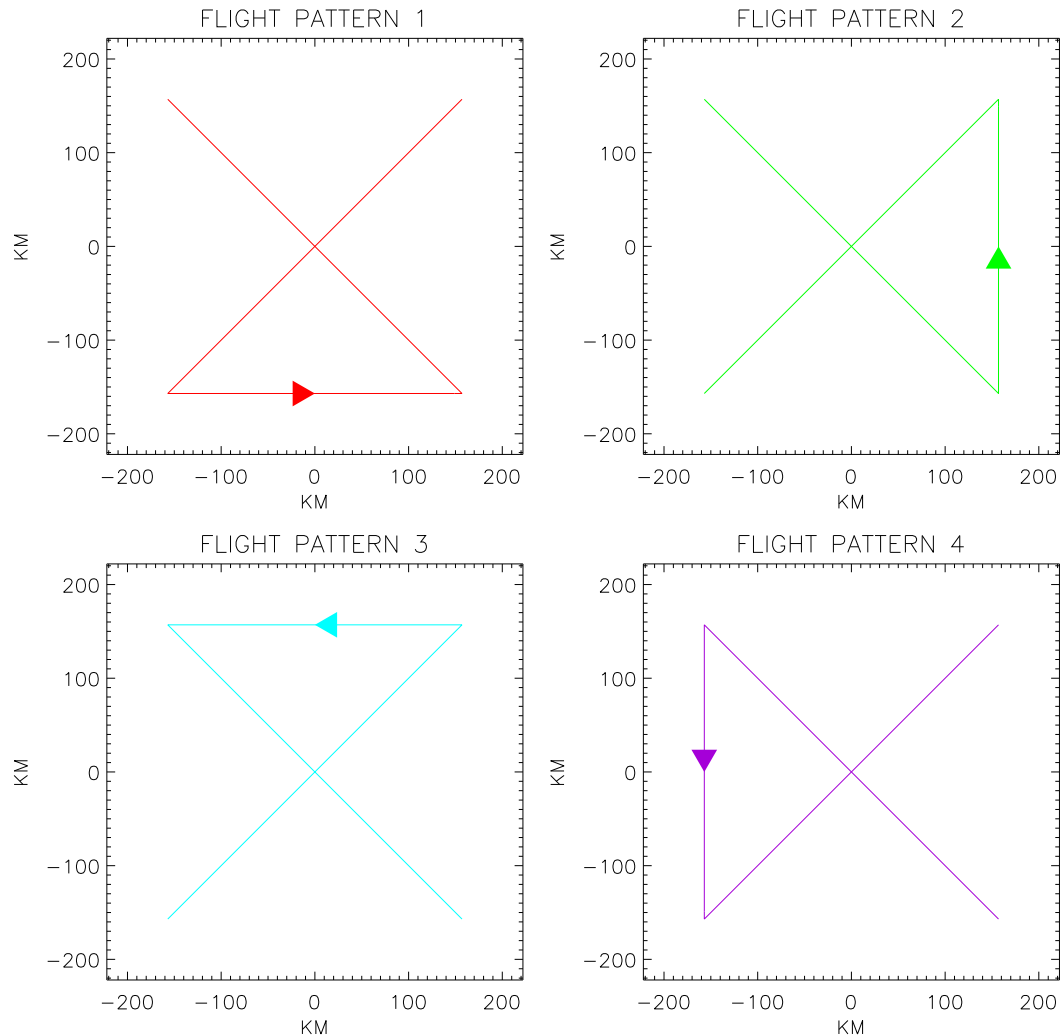| Wavenumbers	WS$_{MAX}$ (m s^{-1})	RMW (km)	AZIM (°)
0:1	28	24	80
0:2	31	22	83
0:3	31	22	83
0:4	30	22	81
0:5	30	22	81
Model	31	22	84

[6] Ibid.

FIG. 12. Plot of the four distinct figure-four flight patterns given the four radial legs. Each pattern is distinguished by which radial leg is chosen as the first inbound leg.

5. Conclusions

The temporal and spatial variability in wind speed analyses was derived from simulated data collected along a typical figure-four flight path utilized by reconnaissance aircraft. We examined the temporal variability of the wavenumber 0 and wavenumber 1 components of the hurricane wind speed field in a storm-relative coordinate system. We attempted to answer the question of how good a representation of the wind speed field is achieved when only wavenumbers 0 and 1 are used given the natural variability of the field in space and time. Two periods were considered: one when the observed storm is in a reasonably steady state over a period of 8 h and the other when the observed storm is changing its internal structure over time by organizing, strengthening, or decaying.

To answer this question, we utilized the current operational hurricane model—Hurricane Weather Research and Forecasting (HWRF) Model—as a nature proxy to provide complete wind speed fields to permit the computation of sufficient wavenumber components to determine how effective a field representation containing only the first two wavenumbers can be. The results suggest that in the SS period, when the model wind speed field changes slowly over the 8 h, each of the hourly model fields closely resembled the mean model field. The ranges of variation for each of the profiles showed that the preponderance of variability over time exists only in the high-gradient wind speed region within the mean model radius of maximum winds, but changes very little outside the radius of maximum wind. The comparison between the model wind speed field at any time and the first few wavenumber representations
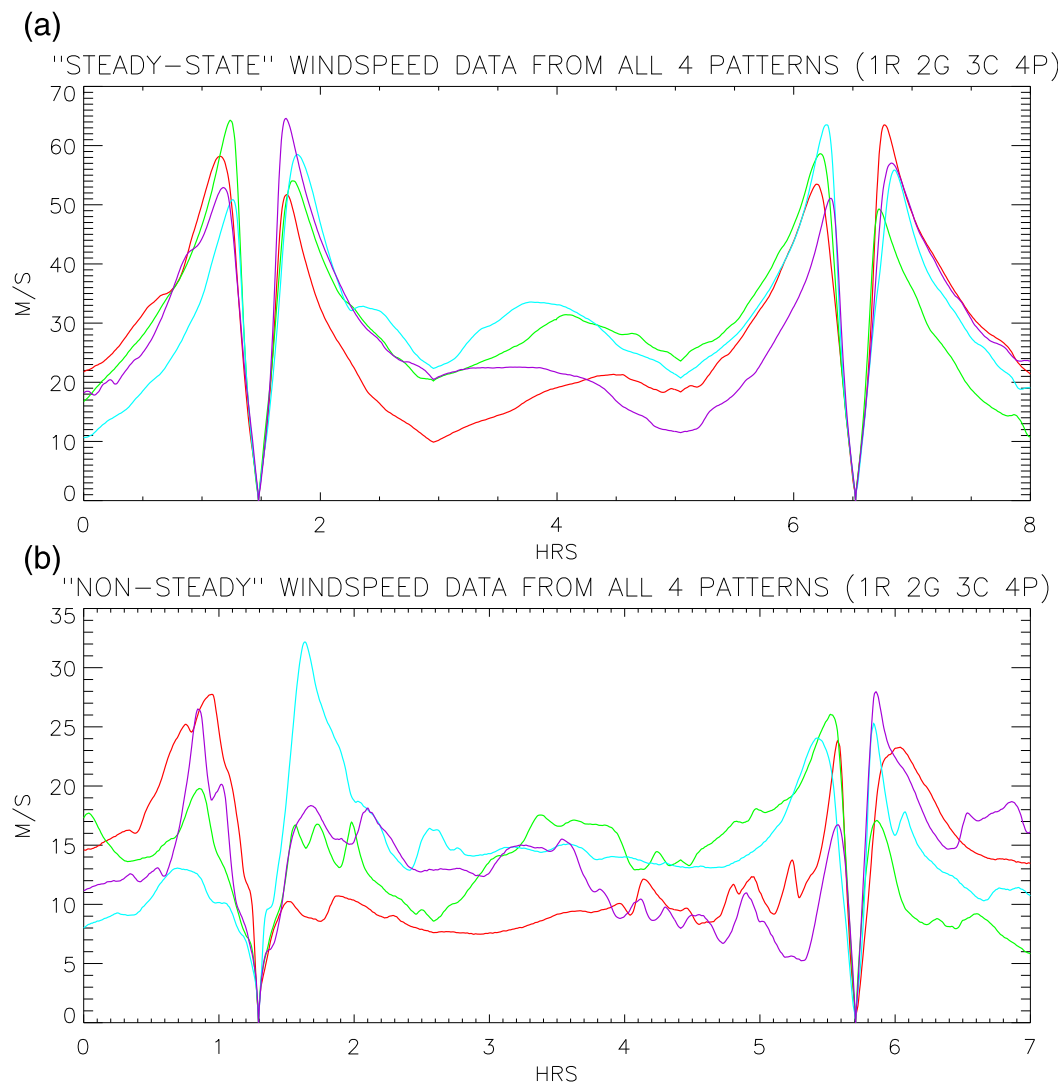
(a)

(b)

FIG. 13. Time series of the collected wind speed data for (a) the SS period (1100–1900 UTC 31 Aug 2010) and (b) the NSS period (1800 UTC 28 Aug–0100 UTC 29 Aug 2010) for each of the possible flight patterns in Fig. 12. The colors represent a different data collection pattern in Fig. 12: red, pattern 1; green, pattern 2; cyan, pattern 3; and purple, pattern 4.

shows that the essential features of the wind speed field (WS_{MAX}, RMW, and AZIM) are captured by the wavenumber (0:1) representation and that including up to wavenumber 3 practically reproduces the model field. However, in the NSS period we find a dichotomy in the rate of convergence of the wavenumber representation sequence to the model wind speed field, and the wavenumber (0:1) representation is inadequate to even capture the essential characteristics of the model wind speed field if the primary circulation is very asymmetric and WS_{MAX} and RMAX are changing rapidly (cf. Fig. 6).

Throughout the NSS period, the mean model wind speed does not resemble any of the hourly instances of

the model field and the ranges of variation among all of the wavenumbers are larger farther from the storm center than the radius of maximum wind of the mean model wind speed. Surprisingly, however, if we include wavenumber 3 in the representation sequence, even the two NSS instances of the model field are described well enough to give reasonable values for the three essential storm characteristics.

In an actual data collection scenario, it takes several hours to collect the data from a single figure-four flight pattern, during which time the storm wind field will be changing to some extent. Moreover, although the four radial legs of the flight pattern are sufficient to determine the radial profiles for wavenumbers 0 and 1, it
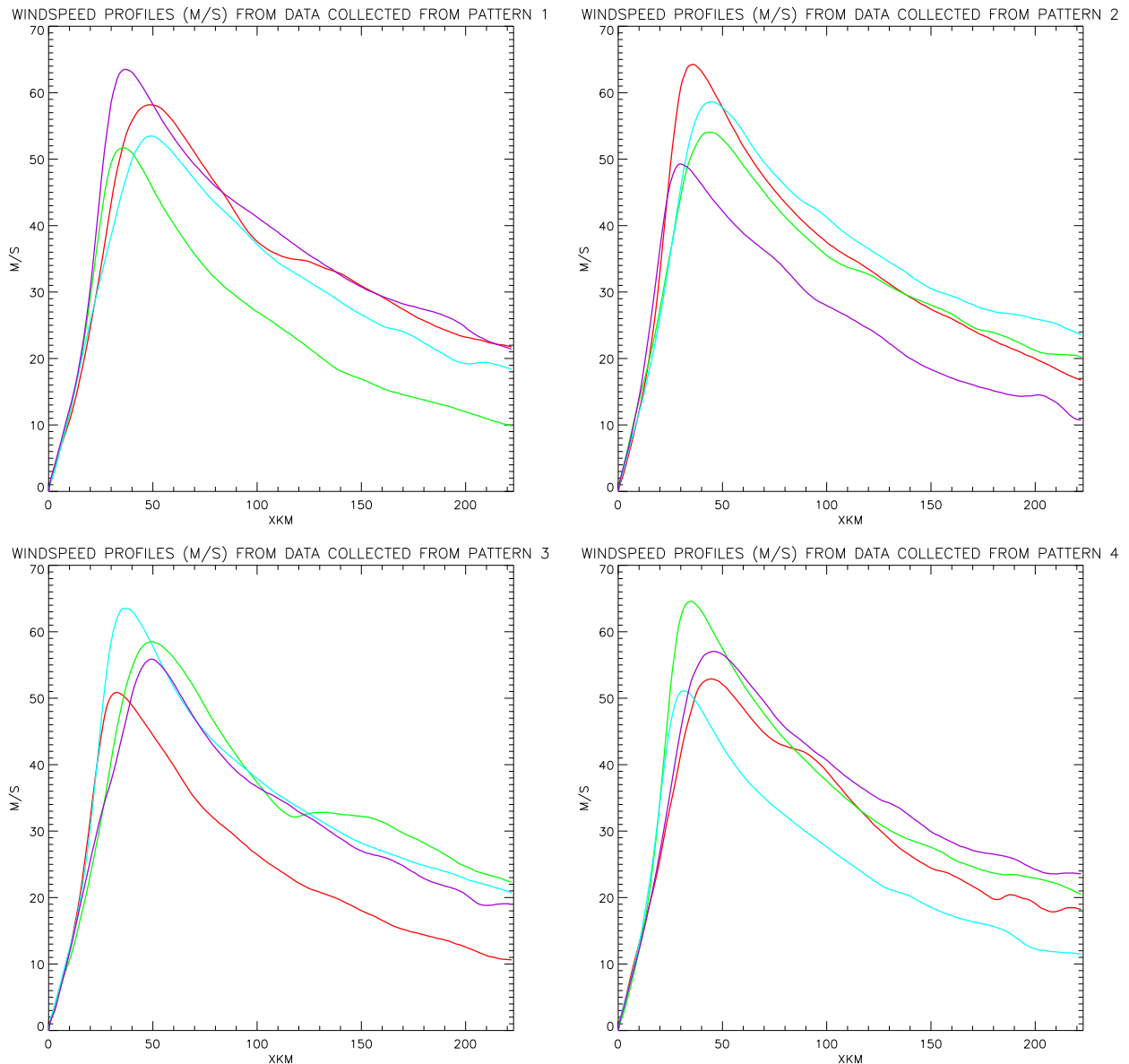
FIG. 14. Radial wind speed profiles for each of the four legs in each of the four data collection patterns in Fig. 12 for the SS period (1100–1900 UTC 31 Aug 2010): pattern (top left) 1, (top right) 2, (bottom left) 3, and (bottom right) 4. Colors depict each of the radial legs: first inbound leg, red; first outbound leg, green; second inbound leg, cyan; and second outbound leg, purple.

must be kept in mind that higher-order wavenumbers will alias onto wavenumber 0 and 1. Even in the best of circumstances where all wavenumbers greater than 1 were negligible, there is still the question of the temporal variability of the radial profiles as they are sampled during the flight pattern.

We attempted to shed some light on the consequences of the temporal variability of the wind speed on the sampling of the data collected over a substantial time interval. During the SS period the characteristics of the wind field retrieved from the

figure-four patterns agrees well with the true wavenumber 0:1 wind field from the model. However, the NSS period exhibited completely different behavior than that shown in the SS example. When the storm is in a near steady state, where the primary circulation is more symmetric and the wind speed field is changing slowly, the storm characteristics obtained from the four different flight patterns bear a substantial resemblance to those obtained from the wavenumber 0 and 1 projection of the model wind speed field. However, if the primary circulation is rapidly
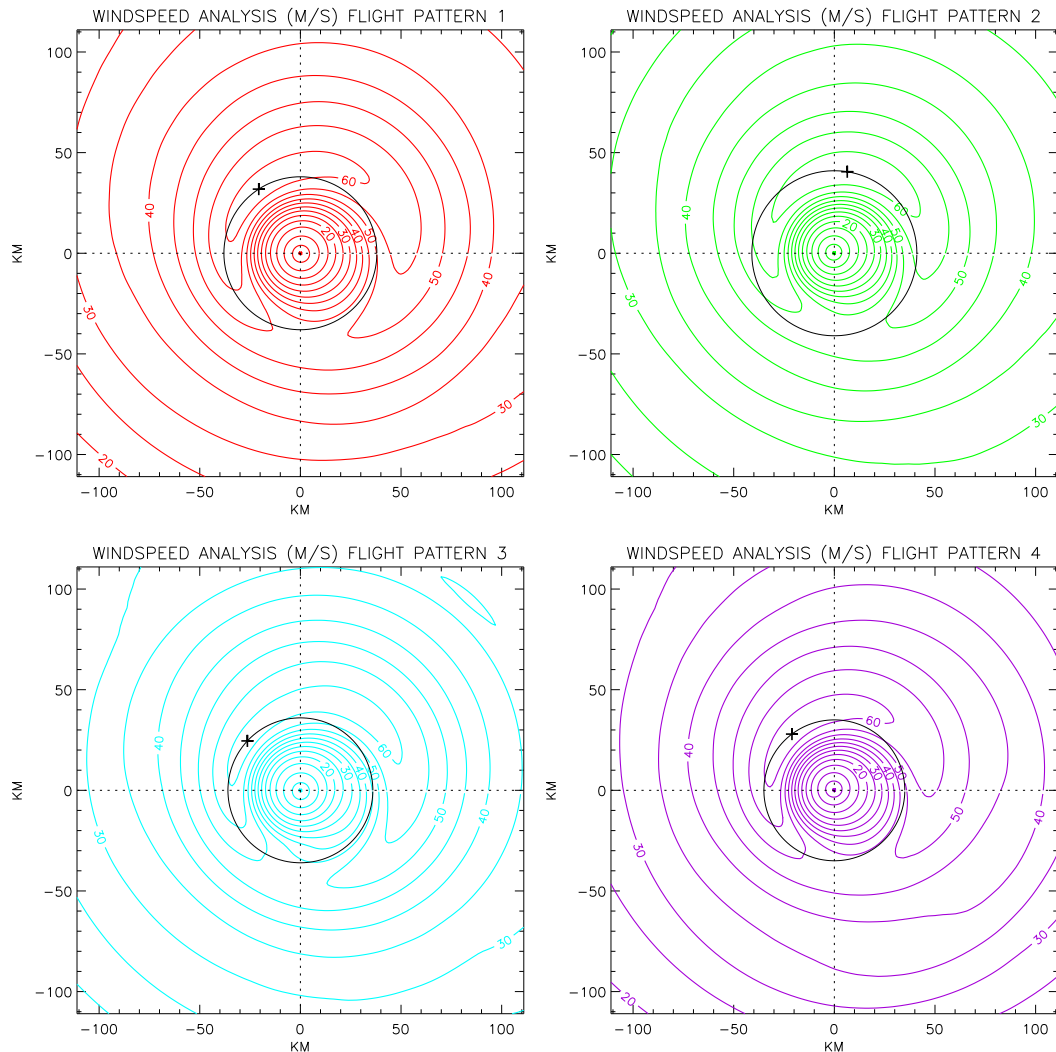
FIG. 15. Wind speed analyses using only wavenumbers 0 and 1 obtained from each of the four data collection patterns in Fig. 12 for the SS period (1100–1900 UTC 31 Aug 2010): pattern (top left) 1, (top right) 2, (bottom left) 3, and (bottom right) 4.

changing in amplitude and/or structure during the data collection period, then the analysis of the wind speed field obtained from the low-order wavenumbers will poorly represent the evolving structure, and contain only a poor representation of the temporal mean structure.

Given the sensitivity of the wind speed field analyses to aliasing from higher wavenumbers when the vortex is asymmetric and rapidly changing, represented by the NSS period, it is likely that our results are also sensitive to the model wind speed field chosen for "nature." As in Vukicevic et al. (2014), our analysis relies on wind speed fields from the operational HWRF model with the smallest horizontal resolution of 3 km on the innermost nest. Choosing a different model with a different resolution or dynamical core could easily alter

the details of our analysis, but likely not the overall conclusions.

TABLE 8. Values of WS_{MAX}, RMW, and AZIM for the four different data collection patterns in Fig. 12 and the wavenumber (0:1) projection of the mean model wind speed field representing the model truth for the SS period (1100–1900 UTC 31 Aug).

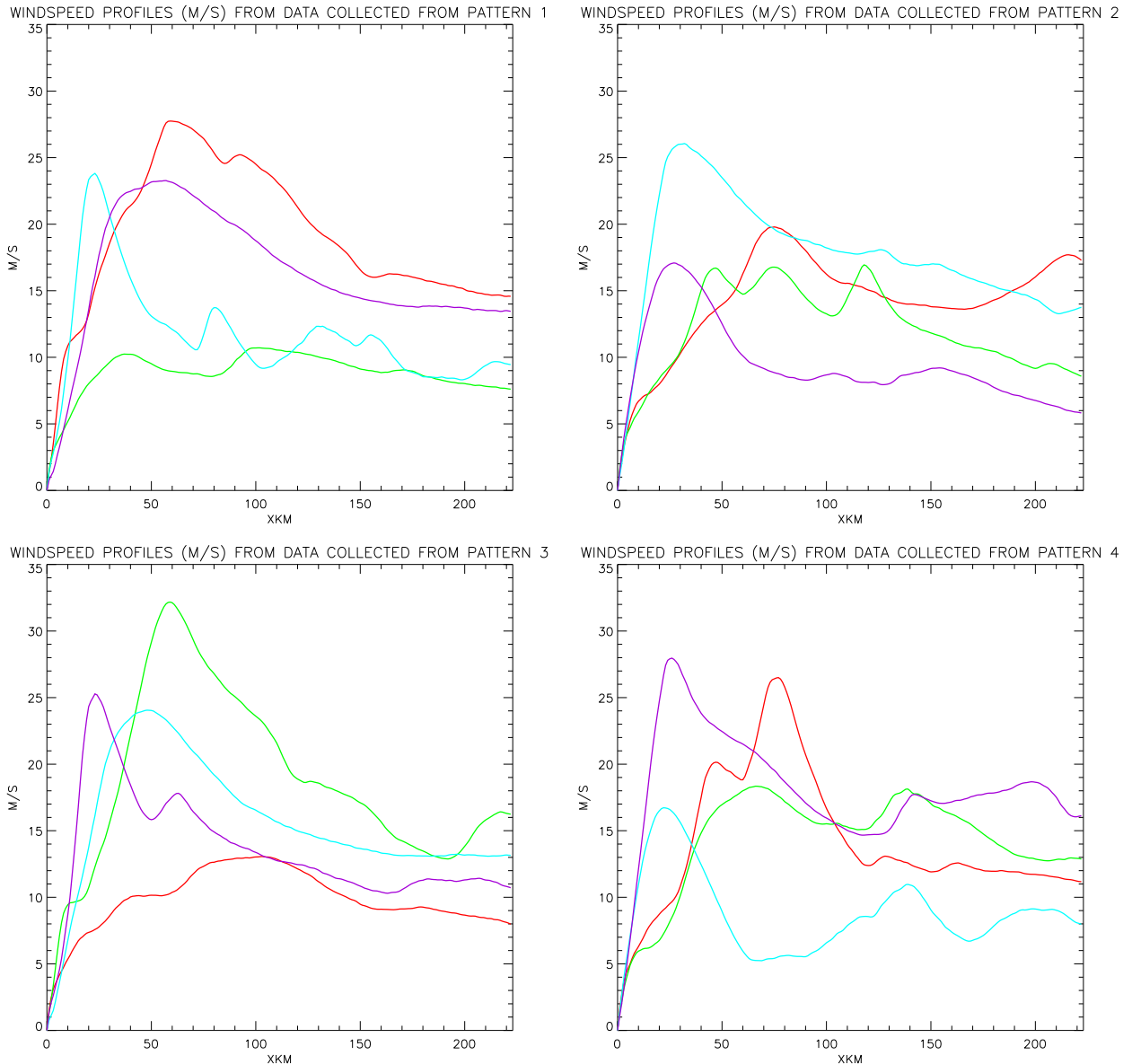| Pattern	WS_{MAX} (m s^{-1})	RMW (km)	AZIM (°)
1	62.0	38	327
2	62.8	41	9
3	61.7	36	313
4	62.4	35	323
Wavenumber (0:1) mean	61.4	39	5

FIG. 16. As in Fig. 14, but for the NSS period (1800 UTC 28 Aug–0100 UTC 29 Aug 2010).

constructive comments on earlier drafts of this paper. The authors were supported by NOAA/AOML's Hurricane Research Division.

APPENDIX

Analysis of the Flight Pattern Data

We present here the method used to analyze wind speed data obtained from a single figure-four flight pattern. For surface winds this would in practice be SFMR wind speed data and perhaps a handful of dropwindsonde and buoy data. The same method could be used to analyze wind speeds at any flight level as long as the data are collected at points along a single figure-four flight pattern.

Figures 13 and 16 depict the wind speed profiles for each of the four legs, for each of the four possible flight patterns. Each profile consists of 223 wind speed values at the time the ''collector'' was collocated with the corresponding point of the corresponding leg of the flight pattern. The along-leg separation of these data is 1 km in space, and 21 or 24 s in time for the NSS or SS periods, respectively.
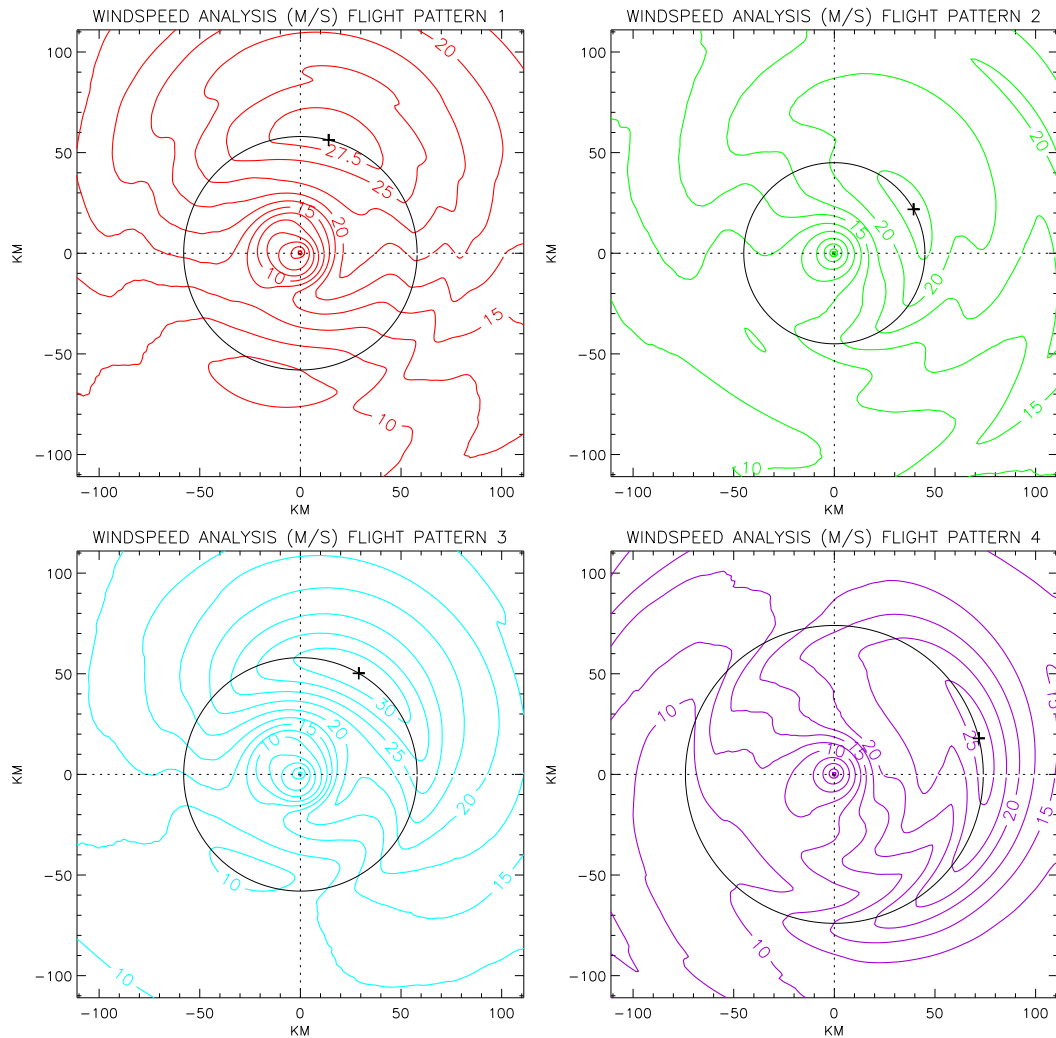
FIG. 17. As in Fig. 15, but for the NSS period (1800 UTC 28 Aug–0100 UTC 29 Aug 2010).

Let $P_k(r)$, $k = 1{:}4$, denote the four profiles, where $0 \leq r \leq 222$ km. The radial basis set generated from these profiles is to be used in the ensuing analysis. We construct the positive definite (in rare instances semidefinite) symmetric matrix,

$$\langle P_i | P_j \rangle = \sum_{k=0}^{222} P_i(r_k) P_j(r_k),$$

where i and j range from 1 to 4, and diagonalize it, obtaining the four eigenvalues $E_1{:}E_4$ and the corresponding eigenvectors $e_{i,j}$. Now,

$$E_1 > E_2 > E_3 > E_4 > 0.$$

From the components of the eigenvectors, the eigenvalues, and the wind speed profiles, we obtain the eigenbasis:

$$\varepsilon_i(r) = \sum_{k=1}^{4} e_{k,i} P_k(r) \Big/ \sqrt{E_i},$$

where i ranges from 1 to 4, so that

$$\langle \varepsilon_i | \varepsilon_j \rangle = \sum_{n=1}^{4} \sum_{m=1}^{4} e_{n,i} \langle P_n | P_m \rangle e_{m,j} = \delta_{i,j},$$

where i and j range from 1 to 4. This process is called symmetric orthonormalization. It is used primarily to deal with the rare circumstances where the four wind speed profiles are nearly numerically linearly dependent. If one or more of the eigenvalues E_k is very small, then the corresponding eigenbasis functions can be omitted from the analysis.

The analysis consisting of only wavenumbers 0 and 1 is then put forward as the ansatz:

TABLE 9. As in Table 8, but for the NSS period (1800 UTC 28 Aug–0100 UTC 29 Aug).

Pattern	WS_{MAX} (m s^{-1})	RMW (km)	AZIM (°)
1	28.9	58	14
2	23.4	45	61
3	31.8	58	30
4	25.8	74	76
Wavenumber (0:1) mean	25.5	64	25

$$\varphi(r,\theta) = C_0(r) + C_1(r)\cos\phi + S_1(r)\sin\phi,$$

where

$$C_0(r) = \sum_{j=1}^{4}\alpha_j\varepsilon_j(r), \quad C_1(r) = \sum_{j=1}^{4}\beta_j\varepsilon_j(r), \quad \text{and}$$

$$S_1(r) = \sum_{j=1}^{4}\gamma_j\varepsilon_j(r),$$

and the 12 coefficients α_j, β_j, and γ_j are obtained by minimizing the expression,

$$J = \sum_{l=1}^{N}|\varphi(r_l,\theta_l) - WS(r_l,\phi_l)|\Big/N,$$

where l ranges over each point of the flight pattern of which there are $N = 1205$ in our observing system sensitivity experiment. Now r_l and ϕ_l are the distance (km) and azimuth (°), respectively, of the location (in storm-relative coordinates) of the lth collected wind speed value.

The minimization is carried out using the downhill simplex method described by Nelder and Mead (1965), since J represents the average absolute deviation between the data collected and the ansatz ψ. The complete analysis is then obtained from the ansatz $\varphi(r,\theta)$, allowing r and ϕ to vary over the entire range of values available to the model output, namely $0 \leq r \leq 222$ km and $0° < \phi \leq 359°$.

REFERENCES

Chen, H., and S. G. Gopalakrishnan, 2015: A study on the asymmetric rapid intensification of Hurricane Earl (2010) using the HWRF system. *J. Atmos. Sci.*, **72**, 531–550, doi:10.1175/JAS-D-14-0097.1.

Gopalakrishnan, S. G., S. Goldenberg, T. Quirino, X. Zhang, F. Marks, K.-S. Yeh, R. Atlas, and V. Tallapragada, 2012: Toward improving high-resolution numerical hurricane forecasting: Influence of model horizontal grid resolution, initialization, and physics. *Wea. Forecasting*, **27**, 647–666, doi:10.1175/WAF-D-11-00055.1.

Hock, T. F., and J. L. Franklin, 1999: The NCAR GPS dropwindsonde. *Bull. Amer. Meteor. Soc.*, **80**, 407–420, doi:10.1175/1520-0477(1999)080<0407:TNGD>2.0.CO;2.

Landsea, C., and J. L. Franklin, 2013: Atlantic hurricane database uncertainty and presentation of a new database format. *Mon. Wea. Rev.*, **141**, 3576–359, doi:10.1175/MWR-D-12-00254.1.

Lorsolo, S., and A. Aksoy, 2012: Wavenumber analysis of azimuthally distributed data: Assessing maximum allowable gap size. *Mon. Wea. Rev.*, **140**, 1945–1956, doi:10.1175/MWR-D-11-00219.1.

Miyamoto, Y., and T. Takemi, 2013: A transition mechanism for the spontaneous axisymmetric intensification of tropical cyclones. *J. Atmos. Sci.*, **70**, 112–129, doi:10.1175/JAS-D-11-0285.1.

Nelder, J. A., and R. Mead, 1965: A simplex method for function minimization. *Comput. J.*, **7**, 308–313, doi:10.1093/comjnl/7.4.308.

Reasor, P. D., M. T. Montgomery, F. D. Marks, and J. F. Gamache, 2000: Low-wavenumber structure and evolution of the hurricane inner core observed by airborne dual-Doppler radar. *Mon. Wea. Rev.*, **128**, 1653–1680, doi:10.1175/1520-0493(2000)128<1653:LWSAEO>2.0.CO;2.

Tallapragada, V., C. Kieu, Y. Kwon, S. Trahan, Q. Liu, Z. Zhang, and I. Kwon, 2014: Evaluation of storm structure from the operational HWRF Model during 2012 implementation. *Mon. Wea. Rev.*, **142**, 4308–4325, doi:10.1175/MWR-D-13-00010.1.

Uhlhorn, E. W., and P. G. Black, 2003: Verification of remotely sensed sea surface winds in hurricanes. *J. Atmos. Oceanic Technol.*, **20**, 99–116, doi:10.1175/1520-0426(2003)020<0099:VORSSS>2.0.CO;2.

——, and D. S. Nolan, 2012: Observational undersampling in tropical cyclones and implications for estimated intensity. *Mon. Wea. Rev.*, **140**, 825–840, doi:10.1175/MWR-D-11-00073.1.

Vukicevic, T., E. W. Uhlhorn, P. Reasor, and B. Klotz, 2014: A novel multiscale intensity metric for evaluation of tropical cyclone intensity forecasts. *J. Atmos. Sci.*, **71**, 1292–1304, doi:10.1175/JAS-D-13-0153.1.